Atomic scale characterisation of the Ni-Al(100) surface and preliminary investigation into it's viability as a template for Zn-Pc thin film growth

A DISSERTATION SUBMITTED TO THE DEPARTMENT
OF PHYSICS OF THE UNIVERSITY OF LIVERPOOL
IN PARTIAL FULFILLMENT OF THE REQUIREMENTS
FOR THE DEGREE OF MASTERS IN PHYSICS

Author: Alan-Francis Kirby (ID: 200895120)
Supervisor: Dr Hem Raj Sharma
April 2016

Abstract

Two materials of technological importance are the ordered Ni-Al alloy and the metal-organic semiconductor Zn-Pc. The Ni-Al(100) surface was investigated by LEED and STM and found to posses a surface of equal parts Ni and Al arranged in an alternate diagonal row structure with 76 % of steps being between layers of like species and 14 % being between layers of different species, with respect to the ideal bulk termination. The sample was annealed at $\sim 800\ K$, resulting in a C($\sqrt{2}$ x $3\sqrt{2}$)R45° reconstruction, with an alternate P(3 x 3) unit cell. The surface displayed no ripple relaxation and furthermore exhibited potential signs of friedel oscillations. The Zn-Pc molecule was successfully deposited at room temperature onto the Ni-Al(100) surface and shown to display an energetic preference to lie flat against the substrate, with one of two distinct orientations with respect to the substrate. The Zn-Pc thin film displayed no long range order for coverage's in the range 0.05-1.88 ML.

Contents

Acknowledgements

Firstly I would like to thank my supervisor Dr Hem Raj Sharma for providing me the opportunity to work in his lab and also for all guidance given throughout the project. I would also like to thank the labs post-doc Dr Abdullah Al-Mahboob for all of his work and knowledge that have contributed greatly to this project. I would also like to thank PhD student Samuel Coates for support and guidance during the project and for his work contributing to this project. I would finally like to thank the department of physics at the university of Liverpool for allowing me to complete my masters degree with them.

Declaration

I Alan-Francis George Kirby, confirm that the work submitted in this thesis is my own, and that appropriate credit has been given wherever reference is made to the work of others.

Signiture: ______________ Date: ______________

Chapter 1

Introduction

1.1 Premise of the Research

Condensed matter physics is the branch of physics where we often observe strange phenomena due to the strong correlation between particles, but where experimental investigation into the underlying physics does not typically[1] require the application of large scale multinational collaborative experiments, as is required in particle physics. Much of the research within condensed matter physics is driven by real world applications, and thus unsurprisingly the properties of various materials are widely researched. It is often the case that it is desirable to have a material with various characteristics that often don't coincide together, such as low rigidity, high conductivity and yet remaining cheap to obtain and easy to use in a manufacturing process[2]. Therefore much of the current research in condensed matter physics[3] is focussed on alloys and thin films, where the different components can contribute separate characteristics. Alloys are typically utilised applications requiring the likes of low density and high strength materials, whereas thin films are often employed for antimicrobial and antireflection coatings [1–3]. Thin film research does indeed have many implications for the modern technological world, however the research also has benefits for the purely academic arena, enabling investigations into quantum size effects such as film stability for certain film thicknesses, and magnetic phenomena such as Giant Magneto Resistance. Subsequently it may be both instructive and beneficial to combine such materials and form a thin film on an alloy substrate.

Within condensed matter physics, the electron and proton are the fundamental fermions and the photon is the fundamental boson, with the interactions on the relevant length and energy scale being governed by quantum electrodynamics [4]. Within a thin film, the electron wave function is confined between the two surfaces of the film resulting in oscillations in the density of states at the Fermi energy. These oscillations in the density of states influence the total energy of the thin film and all associated properties such as the magnetic susceptibility and the electrical and thermal

---

[1] It is however true nonetheless that many experimentalists in condensed matter physics nowadays make frequent use of large scale facilities such as those at Diamond light source and ISIS, both located in Oxfordshire, UK.

[2] These are some of the properties required by flexible circuits for next generation electronic devices.

[3] Specifically within surface physics, as a sub field of condensed matter physics.

conductivities, and thus the size of the thin film may influence its properties [3].

The crystal structure of the substrate is an important consideration for heteroepitaxy due to the consequences for the crystal structure of the resulting thin film. The crystal structure of the thin film inevitably influences the potential experienced by the electron gas due to the periodic ions of the crystal lattice, thus influencing the total energy of the thin film and all related properties such as electrical and thermal conductivity. Moreover it is not only the dimensions of the thin film that influence its properties but also its atomic arrangement, and thus the choice of substrate is an important consideration in the formation of these new materials.

Organic molecular films have become increasingly important over the last few years being used in various optical and electrical devices such as organic field-effect transistors and organic light emitting diodes. Such devices could not have been easily fabricated using single crystals due to crystal size limitations, poor mechanical strength and difficulty in processing [5]. An organic molecule of recent interest for use within various electronic heterostructures is zinc-phthalocyanine (Zn-Pc). Likewise the complex metallic alloy Ni-Al has been the subject of much investigation as a consequence of its low density and high strength. The characteristic features and common applications of both of these materials is outlined below in section 1.1.1 and section 1.1.2. To the author's knowledge, there is no literature reporting the growth of crystalline Zn-Pc on the Ni-Al system despite the potential future applications of such a material. Moreover it will be the subject of this work to initiate a preliminary investigation into such a system, in the hopes of potentially expediting future development of such materials.

The presented work will adhere to the following format; motivation for the work and all background knowledge required will be presented in chapter 1, the experimental set-up along with the methodology and results will be contained within chapter 2, the analysis and discussion of the results will be provided within chapter 3, the conclusions of the work carried out and an outline of the future work will be discussed in chapter 4, whereas any additional remarks will be provided within the footnotes, or where appropriate will be provided within an appendix.

1.1.1 The Zn-Pc Molecule

Phthalocyanine's (Pc's) are planar aromatic macrocycles which form an organic semiconductor composed of self-assembling liquid crystals. The discovery of Pc's in 1928 was somewhat serendipitous, nonetheless their discovery has since resulted in many applications including; dyes for both inks and textiles, information storage devices, liquid crystal displays and organic solar cells [2]. Furthermore Pc's possesses many desirable physical traits for technological application including high chemical and physical stability, their electronic properties, significant absorption for visible electromagnetic radiation and their capacity to withstand intense electromagnetic radiation[6]. Complementary to the physical traits of Pc's is their versatility. The two central hydrogen atoms enable the incorporation of over 70 metals with various substitutions also possible which subsequently provides the means to fine-tune the properties of the substance. A model of the metal-phthalocyanine system is provided below in fig. 1.1, where the Phenyl rings[4] are each composed of six carbon atoms, five of which are bonded to hydrogen atoms and have been omitted from the model.

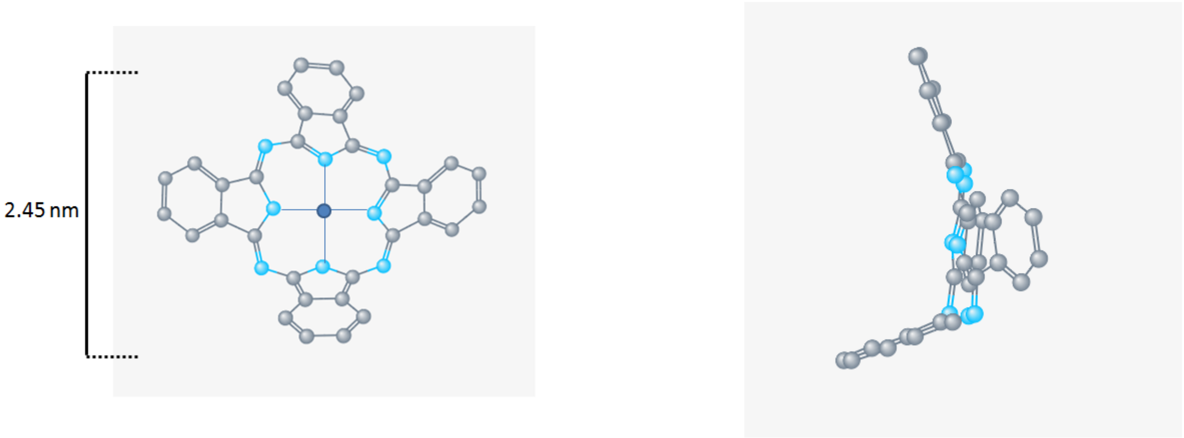

(a) Front view. **(b)** Side view.

Fig. 1.1: Showing a model of the metal-Pc molecule with; Nitrogen (light blue), Carbon (grey) and the metal (dark blue) [7].

Metal-Phthalocyanine's (MPc's) have been investigated since the 1930's and have since been utilised for such technological applications as chemical sensors, bioelectronics, catalysis, quantum dot technology and in clinical research utilising photodynamic therapy [8, 9]. Furthermore phthalocyanine's possessing a metal centre have been researched extensively for their application in heterojunction organic photovoltiacs. The first[5] reports in 1986 demonstrated efficiencies of 1 %, with current efficiencies around 6 % [11].

A significant candidate for photovoltaic and other electronic applications is Zn-Pc, owing to a 1.97 eV direct band gap, high absorption coefficient in the visible part of the electromagnetic spectrum with peak absorption at 330 nm (relating to the B band) and 690 nm (relating to the Q band), whilst being easy to synthesise and yet non-toxic [6]. The Zn-Pc molecule is not completely flat, however it's exhibited geometry does result in two distinct possible orientations of bonding to a surface, being essentially flat[6] or stood unright.

1.1.2 The Ni-Al Complex Metallic Alloy

Nickel-Aluminium is an ordered binary alloy with a body-centred cubic (BCC) bulk structure, which can be considered as two interpenetrating simple cubic (SC) lattices of Ni and Al, with one lattice displaced by one half of the diagonal of the other. With regards to the BCC structure, the central atom can be taken to be either Ni or Al, with the opposite species occupying directly the surrounding SC lattice sites; thus Ni-Al is isostructural to Cs-Cl (B2 structure). A bulk Ni-Al model produced using the VESTA™ software[7] is given below in fig. 1.2.

---

[4] The four outer hexagonal rings.

[5] It should be noted that their application for organic semiconductors was realised earlier, in 1948 [10].

[6] As displayed in fig. 1.1a, if taken to be from a birds eye perspective of the molecule on top of a substrate.

[7] Visualisation software for aiding electronic and structural analysis.

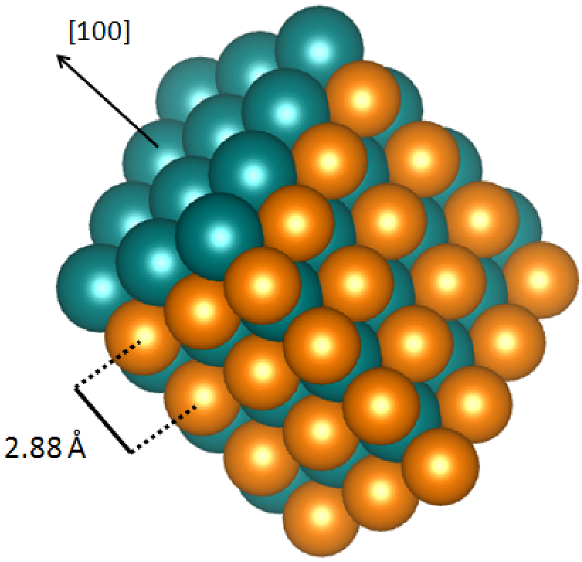

Fig. 1.2: Showing a model of the NiAl bulk structure, where Al is displayed in blue and Ni is displayed in orange.

There exists a wide scope of applications for Ni-Al ranging from; oxidation and corrosion resistant coatings, electronics including semiconductor applications[8] and thermocouple's and also alternative energy structures such as turbine blades. Moreover the Ni-Al alloy's of various composition possess characteristics that are complementary to such diverse applications including but not limited to; good thermal shock resistance, high oxidation resistance, increasing yield strength with increasing temperature, high melting point, high thermal and electrical conductivity, low density and good chemical resistance [1]. In the context of applying Ni-Al as a substrate to template the growth of thin films, the chosen interaction interface will determine the structure of the film and it's resultant properties.

Ni-Al is a prototypical case of a binary metallic alloy in which bulk truncation is typical. This is characteristic of most ordered crystalline alloys[9] and is a consequence of the magnitude of the attractive forces between the two different species[10] [12]. The low index planes of Ni-Al express various preparation dependant characteristics. The (110) surface is an exemplary case with a composition of equal parts Ni and Al where the two species are coplanar and form a rectangular unit cell when bulk terminated [13]. However they are typically displaced relative to their ideal bulk position. This is mediated by species dependent surface relaxations whereby the Al is displaced outwards and the Ni is displaced inwards, resulting in a rippled relaxation of the surface. The extent of this relaxation is dependant on the chemical environment which is determined by the level of; surface segregation[11], surface reconstruction and defect creation enabled by the preparation conditions [12, 13].

---

[8] Recall that phthalocyanine is a semiconductor.

[9] As opposed to random alloys which are also known as solid solutions or disordered alloys, in which the occupation of each species onto the lattice sites is of a statistical nature.

[10] For solid solutions, these forces are too weak to inhibit surface segregation of one of the species at thermal equilibrium; thus enabling surface reconstruction.

[11] Surface segregation can also influence the stoichiometry of the surface.

The (111) surface also demonstrates such surface rippling and furthermore is such that parallel subsurface layers are alternately purely composed of Ni or Al forming a ...A-B-A-B... stacking sequence, consequently enabling Ni or Al termination. The Ni and Al layers each form hexagonal unit cells for bulk termination. It has been established that both domains in which pure Ni or Al layers terminate the surface occur; corroborated by various experimental techniques [12, 14, 15]. Contradictory observations of solely pure Ni termination have also been reported and are reconciled by consideration of the corresponding preparation conditions [16].

The final low index plane, is the (100) surface which posses the same stacking sequence of ...A-B-A-B... as the (111) plane, however with both the Ni and Al layers each forming a square unit cell for bulk termination. The (100) surface may be bulk terminated by pure Ni or Al layers, however early literature suggested solely Al termination [13]. Later work elucidated that a mixed termination appeared to be energetically preferable, suggesting that the pure Al termination is metastable [17]. These divergent observations are again rectified by the acknowledgement of the differing preparation conditions, namely the annealing temperature and quenching rate. A simplistic consideration involves the dependance upon these parameters of both the segregation rate and the ability of the atoms to overcome the local minimums potential barrier. That is to say, that the capacity of the surface to form a lower energy system is dependant on; the capability of the constituents from the first few subsurface layers to diffuse to the surface, and on the ability of the surface layer to redistribute into the energetically preferable global minimum. Reiterating, the Ni and Al surface atoms may be essentially stable within a local minimum, however given the opportunity they may conspire to reposition and establish a globally lower energy configuration. This surface free energy minimisation is principally the reason for the various possible terminations, with a higher annealing temperature enabling a more significant reconstruction[12]. Alternatively one could consider that the balancing of the attractive forces between the different species, and those which provide a mechanism for preferential surface segregation is ultimately what determines the surface termination [17, 18].

The work presented will focus on the Ni-Al(100) surface, as to the authors knowledge there are no reports of such static surface ripple effects associated with this surface; thus presenting a potentially flat surface as a template. There have also been observations of friedel oscillations on the Ni-Al (110) surface [19]; such oscillations may influence the viability of the surface as a template for thin film growth. Thus it may prove instructive to search for similar surface features on the (100) surface to elucidate the nature of the circumstances under which these oscillations will occur and whether they are potentially characteristic of the rippled Ni-AL surfaces. Moreover it will be essential to characterise the surface of the Ni-Al sample used in order to understand the resulting behaviour of the Zn-Pc molecules. A VESTA™ model for bulk terminated Ni-Al is displayed below in fig. 1.3.

---

[12] It should of course be noted that it is thus also possible to heat a sample such as to initiate an excited configuration, and to then quench the sample rapidly (still crystalline) so as to prevent the forming of the global minimum energy configuration; or simply to present a higher energy local minimum than that experienced before the annealing process.

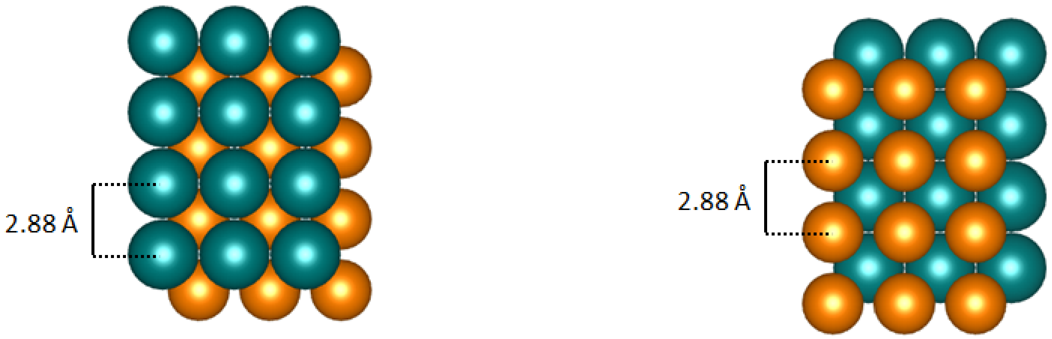

(a) **(b)**

Fig. 1.3: Showing from a birds-eye view a model of the Ni-Al (100) structure, Al terminated in **(a)** and Ni terminated in **(b)**.

It has been reported that a long annealing below 500 K produces a defect enriched Al terminated surface, whereas flash annealing at 1400 K followed by rapid cooling at ambient temperature results in a near perfect Ni terminated surface. Annealing at the interval $500 - 800$ K has been observed to produce a missing row structure with Al termination and a C($\sqrt{2}$ x3$\sqrt{2}$)R45° corresponding LEED pattern [20].

1.1.3 Friedel Oscillations

Somewhat simplistically, friedel oscillations are related to oscillations in the local density of states that are often observed within scanning microscopy images. They are typically observed when the wavefunction of the tunneling current scatters from point defects on the surface. The corresponding wavelengths of these oscillations is typically of the order of several nanometers, with the oscillation decaying exponentially away from the defect. Such defects on substrates are of interest to the growth of thin films, as the resultant interaction between the film and substrate can be influenced by the variation in the electronic structure of the substrate as experienced by the film [21, 22].

1.2 Ultra High Vacuum

The following section presents the necessity for surface physics experiments to be performed under very low pressure conditions and outlines some of the components of the experimental set-up and procedure that are required in order to achieve, work under and monitor such experimental conditions.

Surface physics experiments performed under atmospheric pressure are subject to the rapid formation of layers of contaminant upon the sample substrate. The rate of contamination depends on the incident flux of gas molecules upon the sample surface and on the sticking coefficient. The flux is obtained from the kinetic theory of gasses;

$$Z = \frac{P}{(2\pi MkT)^{1/2}}, \tag{1.1}$$

where Z is the flux in units of $cm^{-2}s^{-1}$, P is the ambient pressure in Pa, M is the mass of the gas molecule in kg, k is the Boltzmann constant in JK^{-1} and T is the temperature in K [3].

The sticking coefficient is the fraction of the incident molecules that adsorb on the surface, and depends upon the temperature, surface structure and the surface coverage. Assuming a sticking coefficient of unity, the time required for the formation of a monolayer at room temperature and atmospheric pressure is of the order of nanoseconds. This is far short of the typical time period required to perform experimentation of 10^4 s , thus necessitating the use of a vacuum. Moreover the pressure required in order to maintain a clean sample surface for this period of time is of the order 10^{-10} $mbar$ and below, which is known as the Ultra High Vacuum (UHV) regime.

Surface physics experiments employ various probes for investigating the chemistry and structure of the sample surface. Ambient gasses typically have mean free paths much smaller than the experimental dimensions of the set-up, resulting in interference of the probe with the ambient gas. Under UHV pressures the ambient gas has a mean free path of 10^6 m, essentially neglecting any interference with the probe particles. Furthermore such a small mean free path results in the gas particles rarely interacting with one another, but rather traversing the chamber and only interacting with the walls. Thus within such a pressure regime it is the walls of the chamber that determines the properties that the gas phase is endowed with [3]. The ambient gas may also interact with the sample substrate either chemically or electromagnetically, furthering the requirement for a minimal ambient pressure and thus the use of UHV. Typical values for the mean free path of ambient gas and the time required to form a monolayer are shown below in table 1.1, demonstrating the requirement for pressures in the UHV regime.

Level of vacuum	Mean free path (m)	Time to form a monolayer (s)
Atmospheric	$7 \cdot 10^{-8}$	10^{-9}
Low	$5 \cdot 10^{-5}$	10^{-6}
Medium	$5 \cdot 10^{-2}$	10^{-3}
High	50	1
UHV	10^6	10^4

Table. 1.1: Showing the mean free path of ambient gas molecules and the time required to form a monolayer, for various levels of vacuum [3, 23].

Typical UHV systems contain several key elements including; monitoring devices for the ambient gas pressure, sample manipulators, sample heaters and coolers, sample view-ports; gas entry systems for sample cleaning and deposition, pumps for gas evacuation and components for analytical techniques.

1.2.1 Pumps

The kinetic theory of gasses implies that two systems of gas that are exposed to one another and isolated from the external environment, will interact such as to establish an equilibrium pressure.

Thus to evacuate the chamber of ambient gas to a sufficient extent requires the use of pumps, which are utilised to transport gas molecules from the system, to the external environment without allowing for a significant occurrence of the reverse process.

The pumps that can operate in atmospheric pressure of 10^3 $mbar$ are the rotary and sorption pumps, which can be used to obtain pressures of 10^{-4} $mbar$. The rotary pump utilises a variable length, spring-loaded rotating vane. The vane allows for the gas to enter the pumps chamber from the inlet, being swept along the chamber and compressed as it reaches the valve, which opens under the higher gas pressure and thus ejecting the gas from the pump. The rotary pump is cheap and durable, however it also produces vibrations and can thus perturb measurements that rely on techniques such as scanning microscopy, often rendering them unusable. The sorption pump possesses no moving components and thus does not present the same issue. The sorption pump uses a highly porous material cooled by liquid nitrogen, to adsorb the gas molecules onto its surface and hence removing them from the system. However this process saturates once the surface area is covered, and may desorb the gas molecules in the event of accidental heating of the pump.

The pumps that can operate in the mid pressure range of $10^{-2} - 10^{-10}$ $mbar$ are the turbomolecular and diffusion pumps. The turbomolecular pump utilises a series of angled blades that rotate at high speed, with the blade direction alternating between each stack. The first stack rotates and results in a momentum transfer to the gas molecule via collision, with the second stack being stationary. The gas molecule thus collides with the blade of the second stack, progressively directing the molecule to the pumps outlet which is typically coupled to a rotary pump. Turbomolecular pumps, just as with rotary pumps contain moving components and thus produce vibrations. The diffusion pump, just as with the sorption pump contains no moving components and produces no vibrations. The diffusion pump uses a jet of heated high speed liquid such as oil to knock the gas molecules out of the pump, and toward a coupled backing pump. A liquid nitrogen trap is also required between the pump and chamber in order to trap the oil molecules.

The pumps that can operate in the UHV range of $10^{-9} - 10^{-12}$ $mbar$ are the Ion and Cryo pumps. The Ion pump composes of no moving components and thus produces no vibrations. The Ion pump utilises an electric discharge between an anode and cathode, ionising the local gas molecules which are then swept to the cathode where they are captured or chemisorbed. The cryo pump uses liquid Helium to condense and trap the gases to be pumped, however this is rarely used due to the low supply and thus high cost of liquid Helium. A schematic representation of the pressure ranges[13] for the aforementioned pumps is displayed below in fig. 1.4.

---

[13] Note that the disparity between the higher pressure stated and that shown in fig. 1.4 for the ion pump is due to the saturation of the ion pump at pressures greater than that stated.

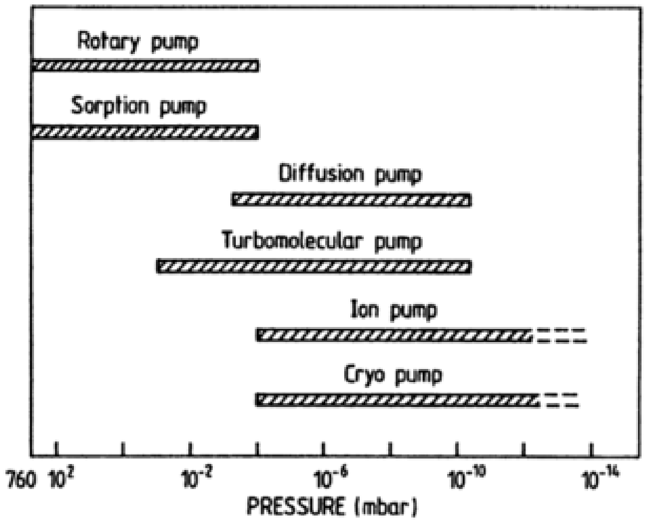

Fig. 1.4: Showing the operational pressure ranges for several types of pump used within UHV experiments [23].

Titanium sublimation pumps (TSP) are often used as an additional support pump. The operation of a TSP utilises a high current passing through a titanium filament to evaporate titanium onto a large surface area. Gas molecules are chemisorbed onto the resulting thin film, and are thus removed from the system. This method is not suitable for nobel gases due to their closed valance shell and thus negligible electronic response with the titanium interface.

1.2.2 Baking

The evacuation of ambient gas from the system is a time consuming task and there are several processes involved. The first of which is the evacuation of the majority of the gas from the volume of the chamber. This is a rapid process, with the gas pressure reducing exponentially. Following this is the desorption of the gas which has adsorbed onto the inner walls of the chamber, followed by subsequent evacuation. This step is slower than the initial evacuation, with a pressure that reduces in a manner inversely proportional to time. The last process involved is the diffusion of the gas that has dissolved into the walls, followed by subsequent desorption and evacuation. This is the slowest stage of all, with a pressure that reduces in a manner inversely proportional to the square root of the time. Finally, UHV is obtained when the majority of the gas has diffused through the walls, desorbed from the walls and then been evacuated from the system, with the lowest pressure being obtained when the diffusion reaches the permeation limit [3].

The time required to obtain UHV from atmospheric pressure with only the use of pumps is of the order of years. Thus the use of UHV would not be practical without an accelerated rate of removal of the ambient gas. Realistic experiments employ the use of baking alongside the operation of pumps, whereby the system is heated to $150-250\ ^{\circ}C$[14]. The thermal energy supplied to the system results in accelerated rates of surface diffusion and desorption. The timescale for obtaining UHV from ambient

---

[14] The temperature may depend on the contents of the system during baking.

pressure is reduced to several days, thus allowing for the realistic requirements of experimentation to be met [3, 23].

1.2.3 Experimental Chamber

The requirement of baking the system necessitates that the system be constructed from materials that can withstand such conditions, owing to properties such as; small thermal expansion coefficient, high melting temperature, high thermal shock resistance and low susceptibility to thermal creep. Furthermore high vapour pressure materials which evaporate at low pressure are not suitable for use with UHV, as they would contaminate the system at the pressures required for experimentation. The chamber and pipework are typically made of stainless steel due to its resistance to corrosion and rusting and also to its low outgassing rate of adsorbed gas. The vacuum joints employ metal seals such as a flat circular copper gasket as they provide a strong seal. Fabricated parts such as the sample holder are often constructed from stainless steel, Molybdenum or Tantalum as they are structurally strong with a high melting point and degas significantly at a low temperature. The cooling system is often constructed from a good conductor such as copper, whereas a high density ceramic may be used as an insulator. The windows are typically constructed from amorphous silica glass, owed to its high melting point, large hardness, high transparency in the visible part of the electromagnetic spectrum and to a low thermal expansion coefficient [1, 3, 23].

1.2.4 Monitoring Devices

Experiments utilising UHV require precise control and optimisation of the system, necessitating that the ambient gas pressure and composition be monitored precisely. The gas pressure is typically monitored in the chamber using an ion gauge and is also monitored within the pumping system using a pirani gauge. The ion gauge utilises thermally emitted electrons that are accelerated from the cathode to the anode and consequently ionise the ambient pressure through inelastic collisions. Moreover the measured current is related to the total number of collisions and thus also to the ambient pressure. The pirani gauge measures heat loss within a wire which loses heat due to collisions with the ambient gas; the heat loss is related to the local pressure. Furthermore the gas species is determined using a quadrapole mass spectrometer (QMS), which can be used to provide insight into the source of any unexpected ambient gas. The QMS uses a filament to ionise the ambient gas which then passes into an electric field for which only certain ions will be able to pass through and arrive at the analyser. The mass spectrum of the gas is determined by varying the applied electric field and measuring the number of ions[15] striking the analyser. A schematic for the ion gauge and QMS are given below in fig. 1.5a and fig. 1.5b respectively [3, 23].

---

[15] Reiterating, for a given electric field and fixed geometry, only certain species of gas will reach the analyser and thus contribute to the measurement.

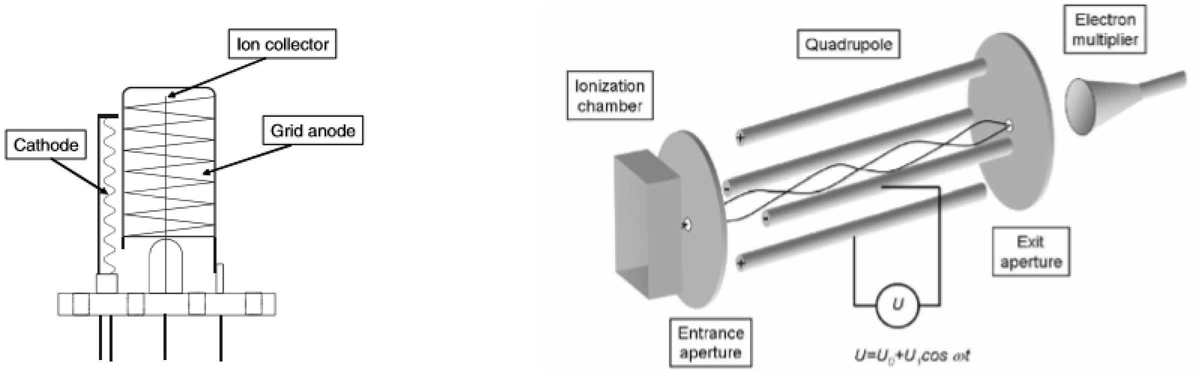

(a) Schematic of an Ion gauge. **(b)** Schematic of a Quadrapole Mass Spectrometer.

Fig. 1.5: Showing a schematic diagram of; **(a)** an Ion gauge, **(b)** a QMS [23].

It should be noted that the QMS can also be used to determine whether the experimental conditions are suitable for various techniques. One such example would be the capacity to anneal at slightly higher than typical pressures. This is possible providing that the majority of the pressure is known to be due to an inert element such as Argon or Hydrogen, as they will not significantly absorb into the sample and result in later surface contamination.

1.2.5 Venting

Experiments often require that part of the vacuum system be exposed to the external environment in order to insert or remove samples and components. The requirement to bake the associated part of the system on every such occasion is not optimal and furthermore often results in an increase of pressure within the sealed part of the system due to the heat enabling desorption of the gas from the chamber walls[16]. Thus the chamber often has a separate loading section which is separated from the main chamber via a valve. This loading section is then flushed when being opened, with an inert gas such as nitrogen, resulting in the inner walls being coated in the inert gas. Inert gasses such as Nitrogen that bond to the chamber walls through physisorption are typically faster to remove during pumping, and they act as a physical barrier to prevent other molecules from bonding onto the surface. This significantly reduces the amount of absorption into the chamber walls and adsorption via chemisorption onto the walls. Moreover this removes the requirement for the chamber to be baked in order to obtain UHV conditions, with solely the aforementioned pumps being adequate [3].

1.3 Sample Preparation

The following section briefly outlines the general procedures carried out in order to prepare a clean crystalline sample for investigation.

---

[16] This could prematurely end an experiment, as the number of particles adsorbed onto the chamber walls is often so great that if they were to all desorb for a chamber with an internal surface area of 1 m^2 and initial coverage of one monolayer, then the total number of particles within the gas volume would increase by ten orders of magnitude [3].

Although the ambient pressure may be in the UHV regime, any sample that has been exposed to atmospheric conditions and then inserted into the system, or indeed any sample that has been within the UHV pressure for several hours[17], will need to be cleaned of all adsorbed and absorbed atoms before any investigation can be performed. Furthermore the surface structure largely determines the materials properties at the surface, thus it is also necessary to ensure that the sample surface has the desired crystallographic orientation for the given investigation. Many surface physics experiments investigate the growth and properties of thin films, whose crystallographic structure may be influenced by using an appropriate substrate.

1.3.1 Crystal Orientation And Polishing

After the crystal has been grown using one of many available techniques such as the floating zone, Stockbarger or Czochralski techniques, the sample is orientated by cleaving or electric discharge. Once the desired surface crystallographic orientation has been obtained, the surface must then be flattened and removed of the majority of defects. This is achieved by polishing the surface with gradually finer grained diamond pastes. However materials composed of softer elements such as silver are not suitable to be polished in this manner, they require a physically softer chemical polishing [1, 13].

1.3.2 Sputtering

After the sample has been polished the surface will retain various defects and contaminant. These are largely removed via ion bombardment by nobel gas ions such as Argon or Helium. The bombarding ions are generated within an ion gun via collision of a free electron with the atoms electron cloud. The impacting and subsequently ionising free electron is produced by passing a current through a filament. The ions are then accelerated to $500 - 5000\ eV$, with the beam being defocussed and covering the entire sample surface, or being rastered over the surface[18]. The nobel gas is fed into the ion gun through a leak valve. The removal of surface adatoms occurs either via direct collision with the ion, from a collision after the ion recoils off of the substrate or from the energy transfer resulting from the collision of the ion with the substrate. The three processes have cross sections of the same order of magnitude, however the cross section for the first two processes decreases slowly with energy whereas that of the third process increases with energy [3]. The cross section for various nobel gas ions are similar, with the principle dependency being on the energy of the accelerate ion. The sputter rate is given by;

$$\frac{dN}{dt} = -N\sigma j, \tag{1.2}$$

where σ is the cross section, j is the ion currently, t is the time and N is the number of contaminant particles [3].

---

[17] Except for where the investigation involves observing how the system evolves over such time periods.

[18] For highly homogeneous sputter rates, a finely focused beam is rastered over the sample surface [3].

Thus the number of contaminant particles decays exponentially;

$$N = N_o e^{-t\sigma j}, \tag{1.3}$$

where N_o is the initial number of contaminant particles [3].

1.3.3 Annealing

Unfortunately, the process of sputtering results in contaminant atoms being pushed into the substrate matrix and in the formation of various surface defects such as surface vacancies. Thus annealing must be performed, whereby the sample is typically heated to $\sim 50 - 60$ % of its melting point, providing thermal energy to desorb the remaining adatoms, enable surface reconstruction to remove the vacancies and to enable the contaminant to diffuse back to the surface. However, contaminants within the bulk may also segregate to the surface during annealing and hence sample preparation typically involves multiple cycles of sputtering and annealing. The sputtering and annealing conditions and the number of cycles required are specific to the sample and its environment during preparation. Annealing is typically achieved using thermionic emission, however for higher annealing temperatures, other methods such as electron beam heating are utilised. It should be noted that annealing may result in several unwanted effects if the temperature is not sufficiently controlled. Examples include; a roughening of the surface caused by bulk evaporation when the sample is heated too rapidly, irreversible surface reconstruction, or even melting at a lower temperature than anticipated due to the local environment of the surface differing from that of the bulk, requiring that the sample be repolished [3].

1.4 Film Deposition

The following section briefly outlines several methods which are utilised to grow thin films.

Thin films are typically grown via either sputtering, chemical or evaporation methods. For each method, the thin film may be grown in a crystalline or amorphous state depending on the rate of cooling[19], which is influenced by the temperature of the substrate.

Chemical methods utilise the reactions of a chemical cocktail to grow a thin film onto a substrate. Such methods are diverse and widely implemented, however they could unfortunately not be employed for this work due to the restrictions of the experimental set-up which is outlined within section 2.1. Sputtering involves the deposition material being eroded via ion bombardment, and deposited onto the substrate under the influence of a radio frequency electromagnetic field. Sputtering is typically used to grow thin films of compounds or alloys, owing to a sputter rate that is equal for all elements whereas the melting point which is of importance in the evaporation techniques, may vary for different

---

[19] Amorphous thin films typically require cooling rates $\approx 10^6 - 10^8$ Ks^{-1} [3].

elements. The set-up for the sputtering method is the more complex of the two, hence evaporation is often used for growing thin films of pure metals and semiconductors. Evaporation involves thermally liberating atoms which are then deposited onto a substrate. The material to be deposited is typically held within a ceramic crucible which is itself surrounded by a resistive metal which then heats the crucible when a current is applied, subsequently melting the material within the crucible. The surface particles then evaporate and traverse the vacuum chamber and are deposited onto the substrate, providing that the separation from the source is less than the mean free path of the particles within the ambient pressure of the system and that the substrate is sufficiently cold [3].

Unfortunately, typical ceramic crucibles are machined into production and inevitably contain many surface imperfections which result in insufficient degassing below the evaporation temperature of the material being deposited. Consequently other means are often employed, whereby for example a thin sheet of tantalum foil is folded into an envelope which can degas fully at lower temperatures.

1.5 Surface Characteristics

The following section briefly outlines some typical surface characteristics which are observed on crystalline samples and considers the underlying reasons for their formation.

Surface defects are typically investigated with scanning probe microscopies as they provide the atomic structure, size, symmetry and shape of the defects. However defects often propagate across the surface too rapidly for such techniques to observe them, and thus diffraction techniques are often also employed. The majority of surfaces prepared in UHV are subjected to various defects, as shown in the schematic of a vicinal surface below in fig. 1.6.

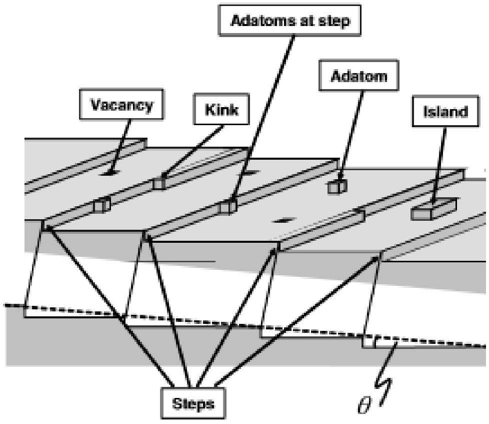

Fig. 1.6: Showing a schematic of various defects on a vicinal surface [3].

The propagation of kinks and adatoms across the surface is related to the minimisation of surface free energy. Moreover the coordination number of an adatom can be increased by diffusing to the step edge or kink, whereas for an atom at a kink or step edge the coordination number can be increased by diffusing to a vacancy site within the terrace. Specifically, any site where the coordination number is greatest on the surface will likely capture adatoms and vacancies. Furthermore the higher the coordination number of the new site, the more likely the atom is to remain their as the amount of work required to break their bonds and free them of their local potential is greater. However when a surface vacancy is large enough the majority of available sites along the length of the vacancy may not provide a higher coordination number than sites at the step edge or kink. Subsequently they may be stable enough to detect with scanning probe microscopy techniques. Kinks in steps form as a consequence of thermal excitation, where the work required to generate the kink for a surface in vacuum is equal to the change in the Helmholtz-free energy. Furthermore it is uncommon for adatoms at a step to remain for a significant period of time as they typically diffuse to a kink site to maximise their coordination number, or they become a kink site to be diffused to by other adatoms [3].

Another consequence of the minimisation of surface free energy is the phenomena of surface relaxation and surface reconstruction, each of which occur in an attempt of the atoms to maximise their coordination number. Surface relaxation involves the surface plane contracting toward the second plane, which itself subsequently contracts away from the third plane. Consequently the planes undergo an oscillatory contraction up to the extent of the selvedge depth. Surface reconstruction on the other hand involves the atoms on in the surface plane increasing their coordination number by pairing off into dimers. The resultant superstructure has a periodicity greater than that of the bulk [3].

1.6 Imaging Techniques

The following section outlines the operation and governing physics for the imaging techniques that were employed within the presented work.

Conventional optical microscopes have been used extensively for scientific enquiry, however they have a poor fundamental resolution limit that inhibits their use in surface physics. The resolution limit is given by;

$$d_{res} = \frac{\lambda_{res}}{2A_N} \sim 250\ nm, \tag{1.4}$$

where d_{res} is the resolution limit, λ_{res} is the wavelength of visible light and A_N is the numerical aperture of the microscope [24]. Thus modern day research requires the use of alternative analytical techniques, such as scanning probe microscopy (STM) and low energy electron diffraction (LEED), outlined below.

1.6.1 Scanning Tunnelling Microscopy

Scanning tunneling microscopy employs a height dependant quantum mechanical tunneling current through a potential barrier in order to map the surface topography of real space with atomic resolution. Fortunately there are no limitations due to sample size or a lack of periodicity on the surface, however the material must be conducting [25].

The five basic components of an STM are the metal tip; the piezoelectric scanner; a current amplifier; a bipotentiostat and a feedback loop. The electrons within a metal experience a finite potential step at the metals surface. The schrödinger equation can be solved on both sides of the metal surface, solutions to which must satisfy the boundary conditions and avoid any discontinuities in the wavefunction or its gradient, at the boundary. It is then seen that the electrons at the Fermi level have a non-zero probability amplitude outside of the metal, which exponentially decays away from the surface. Thus two pieces of metal held at a small separation will experience a mutual tunneling current between one another. These tunneling currents are however equal in their magnitude and thus a bias must be applied in order to achieve a non-zero net tunneling current. The exponential dependence of the tunneling current on the tip-sample separation results in a high sensitivity and thus a high resolution of $< 0.1\ \mathring{A}$ normal to the surface. The resolution tangential to the surface is determined by the sharpness of the tip, with an atomically sharp tip enabling a resolution of $< 1\ \mathring{A}$ [25, 26].

The STM may be used in two modes of operation, those being constant height mode and constant current mode. In constant height mode the tip is scanned across the sample surface with a constant tip-sample separation, with the current being measured as a function of position. The currents dependence on the tip-sample separation thus provides a map of the samples topography across its entire surface via performing a raster scan across it. This mode of operation is fast as the feedback loop is not required to adjust the tip-sample separation, however it is inappropriate for imaging rough surfaces as the tip may collide with the sample. In constant current mode the feedback loop is used to ensure that the current and thus separation between the tip and sample remain constant. The piezoelectric scanner varies its voltage in order to change the tip-sample separation when the surface topography changes, thus maintaining the tunneling current. The piezoelectric voltage is plotted against surface plane position. The result is a map of the samples topography across its entire surface via performing a raster scan across it. This mode of operation is slower than the constant height mode due to the operation of the feedback loop [26].

Rough surfaces are scanned using constant current mode, as the tip-sample separation is maintained and thus the tip will not collide with the surface.[20] Both modes of STM operation may be carried out by applying either a positive or a negative bias between the tip and the sample. A positive bias corresponds to a net tunneling current from the occupied states of tip to the unoccupied states of the sample, and thus the unoccupied states of the sample are being probed. A negative bias corresponds to a net tunneling current from the occupied states of the sample to the unoccupied states of the tip, and thus the occupied states of the sample are being probed. Contaminant on a sample may result in the surface occupied states being unavailable to probe or in the occupied states of the contaminant being probed. Thus in such cases it is preferential to scan with a positive bias such that the unoccupied sample states are being probed, mitigating the influence of the contaminant on the scan. Similarly for biological systems, the sample often possesses surface atoms with a closed

---

[20] The tip may still in-fact collide with the sample in the event of the tip suddenly having poor conductivity due to picking up atoms from the surface, or from a rapid change in surface topography such as at a terrace or island formation site.

valence electron shell, and thus a positive bias is required as there are no occupied states that can be probed effectively.[21] The situation is similar for metals as they have delocalised valance electrons, resulting in a positive bias being most appropriate. STM is however limited to conducting surfaces such as metals, semi-metals and semiconductors, due to the requirement of a tunneling current. The valence electrons of a semiconductor are localised and thus are easier to probe, resulting in a higher resolution being required for metals than for semiconductors, both normal and tangential to the sample surface [3, 25].

1.6.2 Low Energy Electron Diffraction

Low energy electron diffraction utilises Bragg diffraction with electrons as the probe in order to map out the reciprocal space lattice. From the reciprocal space lattice, information regarding the atomic structure and surface morphology of the sample can be obtained.

The basic operation of LEED utilises electrons emitted from a filament and accelerated into a drift tube, which then collide with the sample. The incident electrons that satisfy the Bragg condition are backscattered into preferential directions, with the Bragg condition given by;

$$dsin(\theta) = n\lambda, \tag{1.5}$$

where d is the lattice constant, θ is the angle of scattering w.r.t the normal of the surface, n is an integer and λ is the De Broglie wavelength of the electron [24].

A fluorescent screen is used to collect the backscattered electrons, and is set at a high positive bias in order to accelerate the electrons to sufficient kinetic energy as to enable fluorescence upon impact. The resultant bright diffraction pattern of spots on the dark background due to the elastically scattered electrons are then recorded using a camera and analysed using various software packages such as ImageJ®. In order to satisfy eq. (1.5), the electrons must have a De Broglie wavelength comparable to that of the lattice constant d. The De Broglie wavelength is given by;

$$\begin{aligned} \lambda &= \frac{h}{mv}, \\ &= \left[\frac{150.6}{E_K}\right]^{1/2}, \end{aligned} \tag{1.6}$$

where λ is the De Broglie wavelength in $\mathring{A}$, h is Planck's constant, m is the mass of the electron in kg, v is its velocity in ms^{-1} and E_K is the kinetic energy of the electron in eV [3, 24]. The kinetic energy is given by [24];

$$E_K = \frac{mv^2}{2}. \tag{1.7}$$

Thus for a typical lattice spacing of $\sim 0.5 - 3.0$ $\mathring{A}$, the corresponding electron kinetic energy required

---

[21] It should be noted that scanning biological systems via STM may also result in unwanted damage to the biological sample's surface.

is $\sim 15 - 600\ eV$.

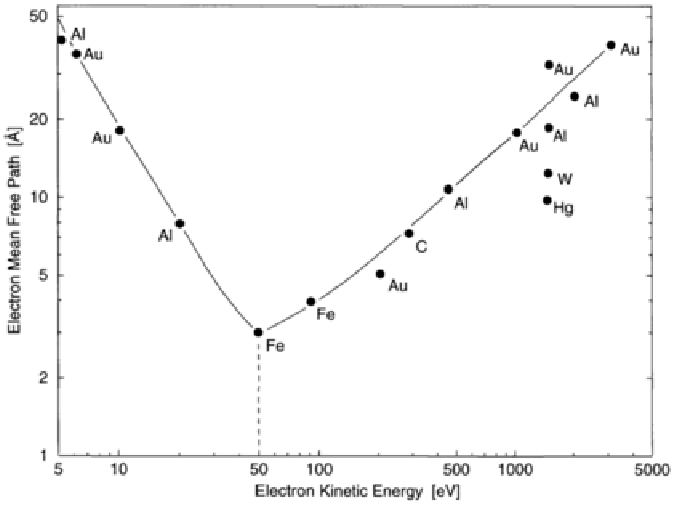

Fig. 1.7: The universal curve for metals, showing the inelastic mean free path of electrons in angstroms vs. the electron kinetic energy in eV.[27]

Electrons of this energy have a small inelastic mean free path of $\sim 5 - 20\mathring{A}$, as can be seen above from the universal curve in fig. 1.7. The inelastic mean free path has a weak dependance on the material and a strong dependance on the electrons kinetic energy. As can be seen in fig. 1.7, for highly surface sensitive experiments an electron kinetic energy of $\sim 50\ eV$ is most appropriate, with a mean free path corresponding to several monolayers [24].

An empirical relationship can be obtained for metals by fitting this universal curve, and is given by;

$$\lambda_{mfp} = \frac{538a}{E_K^2} + 0.41a^{3/2}E_K^{1/2}, \tag{1.8}$$

where λ_{mfp} is the inelastic mean free path of the electron in nm, a is the atomic diameter of the element in nm and E_K is given in units of eV [27].

It is enlightening to further contemplate the consequences of the form of eq. (1.8), which demonstrates that for kinetic energies $> 50\ eV$ the dependence is $\lambda_{mfp} \propto E_K^{1/2}$. Thus the greater the electrons velocity, the larger the mean free path and thus the less surface sensitive our measurements will be. Similarly eq. (1.8) demonstrates that for kinetic energies $< 50\ eV$ the dependance is $\lambda_{mfp} \propto E_K^{-2}$. Thus for such low kinetic energies, electrons are unable to excite inelastic scattering processes such as plasmon excitations, phonon excitations and electron-hole pair formation and are thus inappropriate for use in LEED [24].

The extent of long range order within the sample may be given by the sharpness of the diffraction spots, whereas any point defects will result in a background intensity. The diffraction spots provide the size and symmetry of the surface unit cell in reciprocal space, from which the unit cell in real space can be determined. The surface morphology can be determined from the spot profile. A vicinal surface may be shown through the splitting of fundamental spots into satellite spots, the separation of which is inversely proportional to the terrace width. A facetted surface may be shown through the conglomeration of multiple complete sets of diffraction spots within the final image, each of which is produced by an individual facet.[22] A major limitation of LEED is that it is restricted to application on only ordered structures unlike with STM, however STM requires a conducting surface whereas LEED does not [3, 24].

---

[22] Diffraction spots from different facets can be differentiated from one another, as they move in different directions in response to a change in the energy of the incident beam.

Chapter 2

Experimental Method and Results

The following section is intended to present the experimental set-up used, explain the experimental procedure that was employed, and to present the results of the experiment, for the work presented.

2.1 Experimental Set-up

The experimental set-up used within the work presented composed; a main experimental chamber, a loading chamber, two heating lamps for baking, an ion gauge for the main chamber, a sputter gun with an Argon supply, a thermionic emission heater for annealing, a thermal evaporator for thin film deposition, a QMS for the main chamber, an STM set-up housed within a side chamber and a LEED set-up as analytical methods. The samples and STM tips were manoeuvred throughout the chamber using the magnetic transfer arm of the loading chamber, the manipulator arm of the main chamber and the manipulator claw of the STM chamber. The pumps used for obtaining vacuum were; a rotary pump and a turbo pump for each of the main chamber and the loading chamber, a pirani gauge for each of the turbo pump systems, an ion pump for the main chamber and also a TSP as an additional support pump for the main chamber. Consequently STM scans were typically performed with the rotary and turbo pumps turned off, due to their moving components providing vibrations that produce noise within the scans.

The functionality and workings of the aforementioned components have been discussed within chapter 1. Pictures of the experimental set-up are provided below within fig. 2.1 and fig. 2.2.

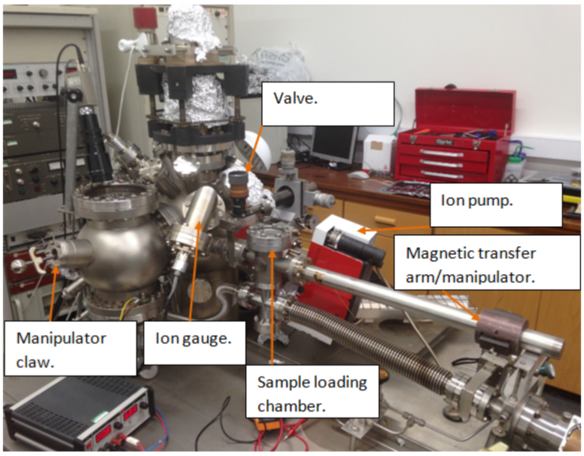

Fig. 2.1: Showing aspects of the experimental set-up.

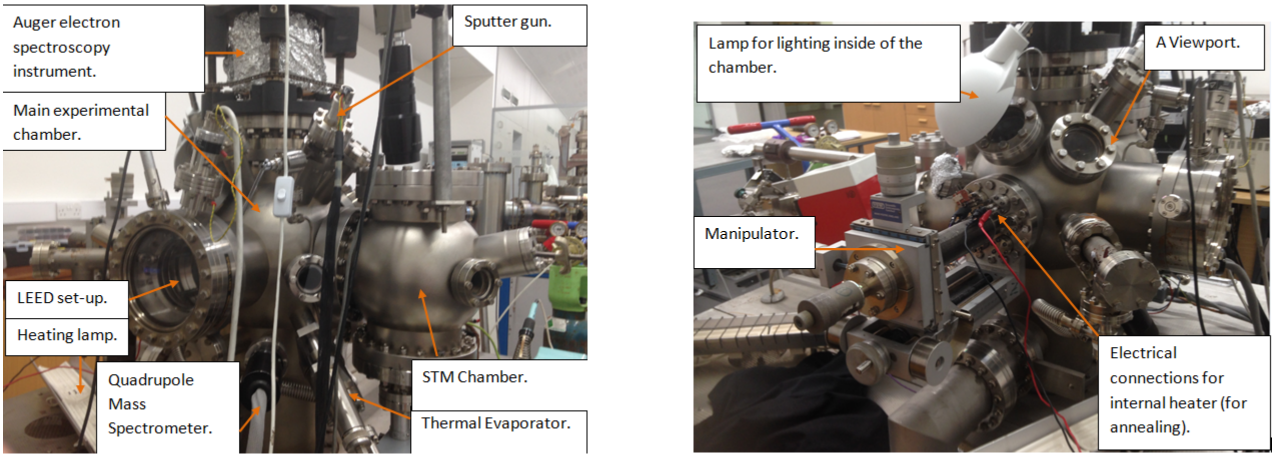

(a) **(b)**

Fig. 2.2: **(a)** and **(b)** both showing aspects of the experimental set-up.

The Auger electron spectroscopy instrument shown in fig. 2.2a was out of operation at the time of the work presented and was thus not used within the investigation. The thermal evaporator employed a tantalum foil as a crucible for reasons outlined in section 1.4. The arm of the thermal evaporator acted to columnate the flux of particles being deposited. The thermal evaporator used a rotatable cover to enable the sample to be heated without presenting a significant flux to the main chamber. The set-up outlined above consistently achieved pressures of down to $\sim 8 \cdot 10^{-10}\ mbar$.

2.2 Investigation of the Clean Ni-Al(100) Surface

The work presented was carried out over a period of several months, so inevitably the experimental conditions and preparation undertaken was not strictly the same for all of the data produced. Subsequently the discussion of the experimentation and the presentation of the associated results is segregated into sections relating to each separate experimental session for which data was successfully obtained. The experimental sessions are presented in chronological order. Data sets A-G relate to the investigation of the clean Ni-Al(100) surface, whereas data sets H-I relate to the investigation of

Zn-Pc thin film growth on the Ni-Al(100) substrate.

The chamber was initially flushed with liquid Nitrogen and then vented in order to replace a broken filament within the sputter gun. Subsequent baking at $\sim 140\ K$ began once the roughening pumps had reestablished a pressure of mid $10^{-5}\ mbar$. After baking for a period of 2 days the pressure was of the order of magnitude $10^{-9}\ mbar$, at which point the TSP was flushed and the ion pump was turned on, whence the system achieved UHV pressures. The Ni-Al(100) sample was polished with progressively finer diamond pastes of 25 nm,10 nm and 2 nm coarseness, and inserted into the sample loading chamber which had been flushed with liquid Nitrogen and vented.

Data Set A

The initial contamination remaining after polishing was removed via two sputter/anneal cycles followed by an overnight anneal at $\sim 300\ K$ in order to ensure segregation of contaminants from the subsurface layers and bulk. Annealing was performed after the initial sputtering so as to prevent any surface contaminant from adsorbing into the bulk due to the thermal energy. The initial sputter was performed at a pressure of $5.5 \cdot 10^{-5}\ mbar$ for 30 minutes, with the second sputter being at the same pressure for a duration of 15 minutes. The initial anneal was performed once the pressure had reached $10^{-10}\ mbar$ in order to prevent adsorption of the contaminant which at that point had been knocked into the volume of the chamber. Each of the two preliminary annealing's were performed[1] at $\sim 500 - 800\ K$, with the first lasting 10 minutes and the second lasting 30 minutes. The cooling time after annealing was 30-45 minutes in all cases.

The sample was then flashed at $\sim 800\ K$ the next morning in order to desorb any surface contaminant and to enable the anticipated reconstruction as outlined in section 1.1.2. The sample was transferred to the STM and images were taken at an initially low bias of 50 mV and 200 mV in order to prevent the tip from potentially locally reconstructing the surface. The resultant images shown below in fig. 2.3 displayed apparent atomic resolution, which was confirmed by varying the scan speed and producing the same pattern. The images display; horizontal noise signatures[2], a large surface vacancy in the lower left region, multiple surface contaminants and moreover a wavy nature in the upper part of the image whereas the lower region is more ordered. The wavy nature within the upper part of the images was observed at both biases and in-fact up to biases of 400 mV, both eliminating external noise as a potential cause of the waves and indicating that this apparent standing wave pattern was stable with time as the images were taken over a period of one hour.

---

[1] The thermionic emission heater had not been precisely characterised before the end of the work, at which point it broke and was replaced. Thus unfortunately a more precise account of the temperature cannot be provided.

[2] See chapter A for a discussion regarding STM image processing and noise signatures.

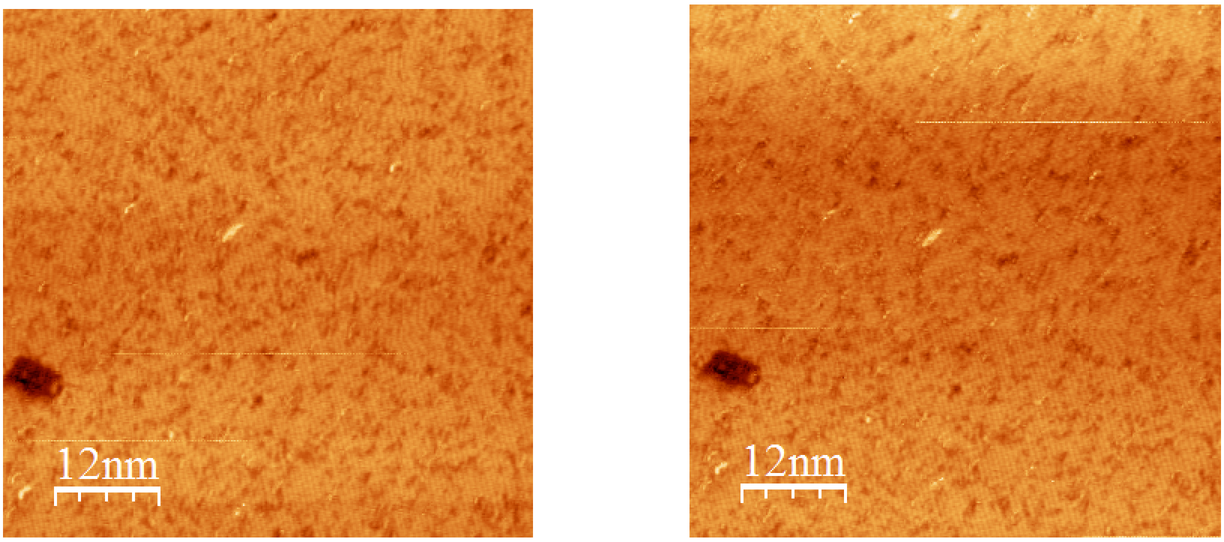

(a) Taken at 50 mV bias and 530 pA current. **(b)** Taken at 200 mV bias and 530 pA current.

Fig. 2.3: Showing atomic resolution STM data of the clean Ni-Al(100) surface, for Data set A.

Scans of steps between terraces were also taken in order to identify the nature of the surface termination by elucidating whether the steps were purely between layers of a single species (2.88 $\mathring{A}$), between alternate species (1.44 $\mathring{A}$) or both[3]. The associated image given below in fig. 2.4a displays; horizontal noise signatures, terraces with 90 degree boundaries, a large surface vacancy in the second terrace from the bottom and defects pinned to the 90 degree boundaries on the third terrace up from the bottom of the image. The image presented in fig. 2.4b is a scan where the tip has been focused in on the surface vacancy that is shown within the second terrace up in fig. 2.4a.

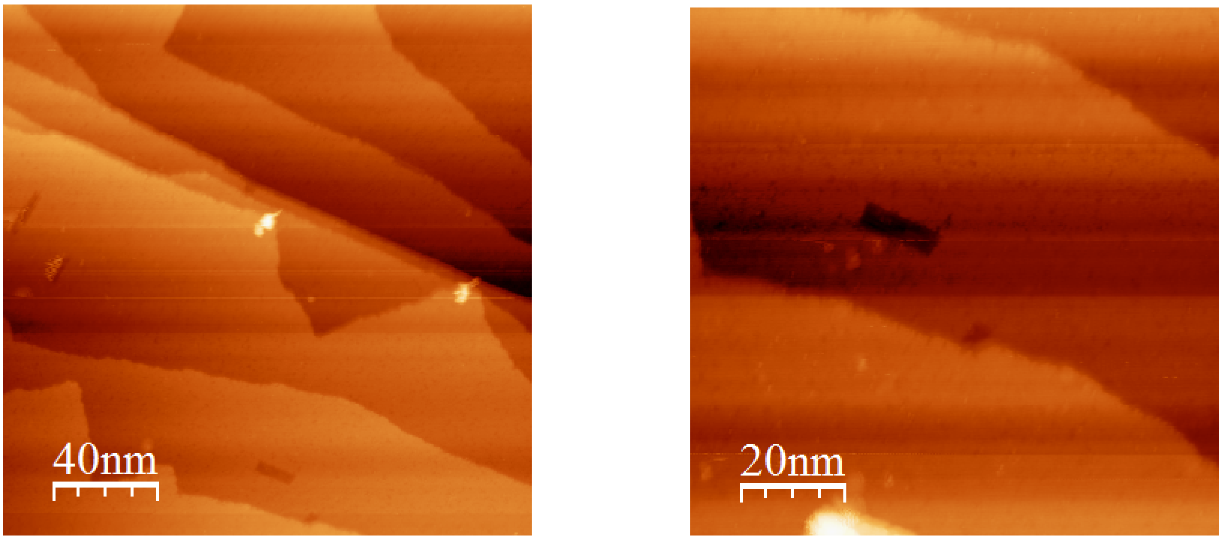

(a) **(b)**

Fig. 2.4: STM data showing terraces of the clean Ni-Al(100) surface, for Data set A.

---

[3] See the model provided within fig. 1.3 for clarification.

Data Set B

The initial high pressure of the order 10^{-9} $mbar$ presented concern for potentially pushing contaminant below the samples surface during sputtering and for generating an over all high enough pressure to cause considerable adsorption of contaminant onto the chamber walls which could later desorb and increase the pressure within the chamber. Thus initially the TSP was flushed in order to achieve a pressure of $2 \cdot 10^{-10}$ $mbar$, at which point four cycles of sputtering, annealing and cooling were initiated. The sputtering was performed at a pressure of $5.5 \cdot 10^{-5}$ $mbar$ for a duration of 25 minutes for the first cycle, 30 minutes for the second and 45 minutes for the final two cycles. The annealing was performed at $400 - 600$ K for the first two cycles and $600 - 800$ K for the final two, all of which were for a duration of 15 minutes with 30 minutes cooling before the next sputtering began. In between the second and third cycles, the sample was flash annealed at $\sim 900 - 1000$ K in order to see whether the sample holder may be degassing as thus contaminating the sample. The pressure remained constant during this annealing and hence there was no apparent degassing occurring.

The sample was then transferred into the STM chamber. Unfortunately due to a poor tip and a noise signature at 300 Hz, no STM images were obtained. The noise signature remained after all pumps and non-essential equipment had been turned off, and in-fact remained for a number of days until it arbitrarily vanished and was subsequently considered as having been caused by an external source. Moreover the sample was transferred to the LEED set-up whence the diffraction image presented in fig. 2.5a was obtained.

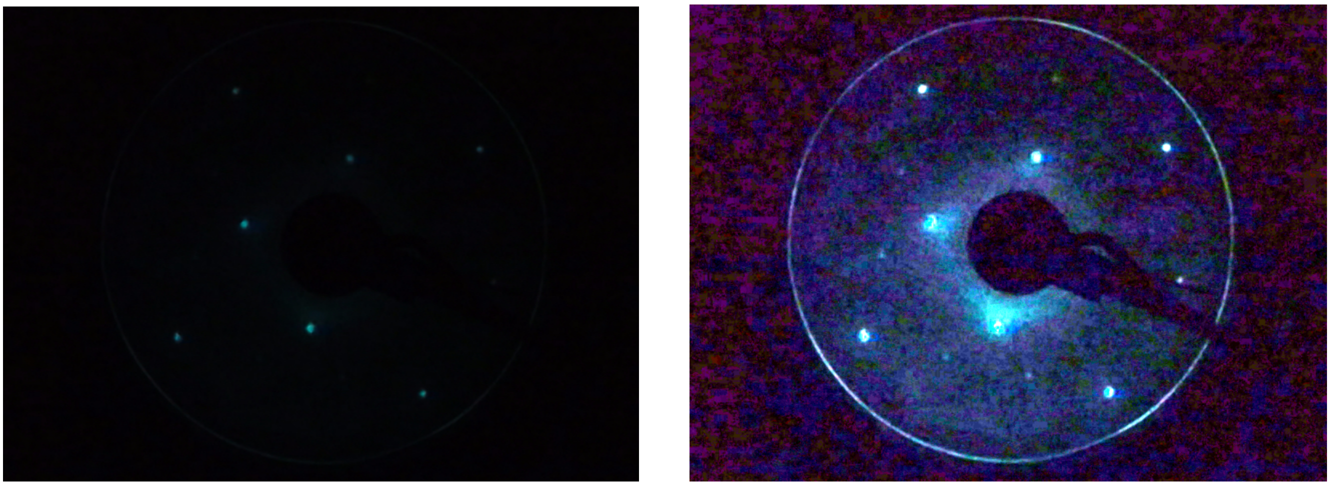

(a) Raw image at 52 eV beam energy.

(b) Manipulated for enhanced contrast.

Fig. 2.5: Showing the LEED data taken of the clean Ni-Al(100) surface, for Data set B.

As can be seen most clearly within fig. 2.5b, the data shows a small 4-fold symmetric square unit cell within a larger square unit cell.

Data Set C

The chamber initially had an excess pressure and thus the TSP was flushed to establish a pressure of $3 \cdot 10^{-10}$ $mbar$. Sample preparation was composed of five cycles of sputtering, annealing and cooling.

The sample was again sputtered first, with all cycles being performed at a pressure of $5.5 \cdot 10^{-5}\ mbar$ for 30 minutes. All annealing cycles were performed for 15 minutes at $600 - 800\ K$, with 45-60 minutes for subsequent cooling. The sample was then transferred to the STM chamber, at which point the image presented below in fig. 2.6 was taken.

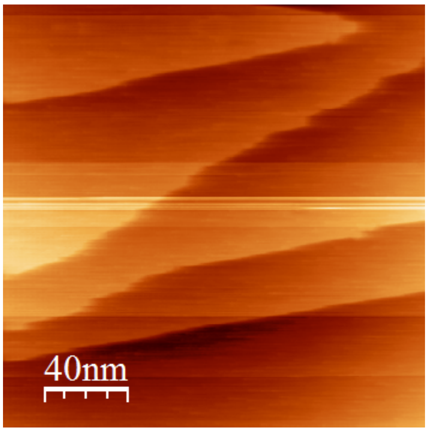

Fig. 2.6: STM data showing terraces of the clean Ni-Al(100) surface, for Data set C.

Unfortunately a significant artifact spanning horizontally across the middle of the image is present, which is generated by a change in conductivity of the tip due to it picking up or releasing contaminating particles[4]. Furthermore the image clearly displays several terraces, although unfortunately the same external noise as experienced for data set B once more conspired to prevent atomic resolution images from being obtained. The underlying source of this noise signature at almost exactly $300\ Hz$ evaded discovery, as the signature once more vanished after several days.

Data Set D

The sample was initially sputtered at a pressure of $5.5 \cdot 10^{-5}\ mbar$ for 30 minutes and then annealed at $\sim 800\ K$ for 15 minutes, with 30 minutes to cool. Subsequently the pressure in the chamber was $8 \cdot 10^{-9}$ and was composed of predominantly hydrogen as shown via the QMS. Consequently the TSP was flushed and the sample was allowed to cool for a further 30 minutes to prevent absorption of any contaminant into the bulk. The TSP was again flushed before each cycle of sputtering. The sample was then sputtered and annealed for two cycles with each sputter being at a lower pressure of $2.7 \cdot 10^{-5}\ mbar$ for a duration of 30 minutes, whereas each anneal was performed at $\sim 800\ K$ for a duration of 15 minutes.

The sample was then transferred into the STM chamber, whence the image provided below in fig. 2.7 was obtained.

---

[4] See chapter A for a more thorough discussion of STM image processing and noise features.

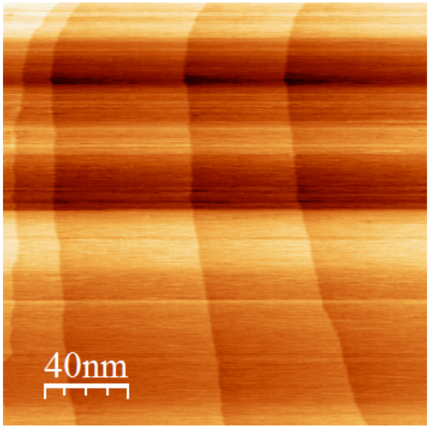

Fig. 2.7: STM data showing terraces of the clean Ni-Al(100) surface, for Data set D.

Unfortunately there are again noise features running horizontally across the image indicating that there may have been high levels of diffusion across the surface, enabling the tip to repeatedly pick up and drop contaminating atoms and thus experiencing a change in conductivity. Furthermore there are clearly distinguished steps within the image, most of which are of a similar size.

Data Set E

The initial ambient pressure contained a large quantity of hydrogen as shown via the QMS. Subsequently the TSP was flushed in order to establish a pressure of $2.5 \cdot 10^{-10}$ $mbar$. The sample was then subjected to five cycles of sputtering, annealing and cooling, with the TSP being flushed between each cycle in order to suppress the hydrogen levels with the chamber. The sputtering was performed at a pressure of $2.7 \cdot 10^{-5}$ $mbar$ for a duration of 30 minutes, whereas the annealing was performed at ~ 800 K for 20 minutes with 40 minutes for cooling. Unfortunately time restriction did not permit the implementation of STM on the day, however the sample was investigated utilising the LEED set-up, the images for which are presented below in fig. 2.8.

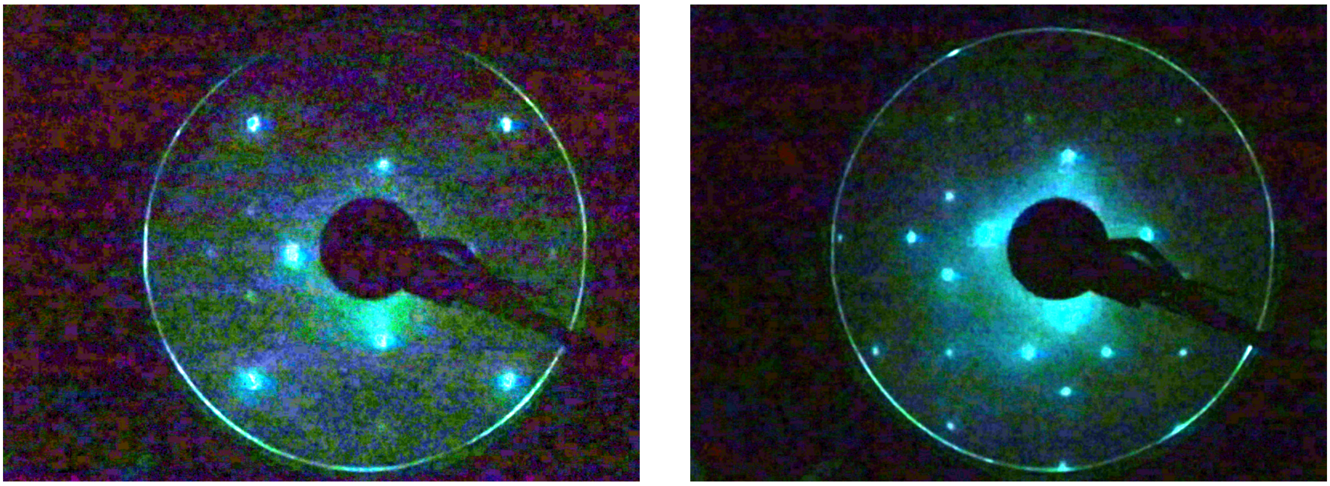

(a) LEED taken at 51 eV beam energy.

(b) LEED taken at 62 eV beam energy.

Fig. 2.8: Showing the contrast enhanced LEED data taken of the clean Ni-Al(100) surface, for Data set E.

The LEED images displayed above in fig. 2.8a and fig. 2.8b have each had their contrast enhanced for the readers clarity. Furthermore both images clearly display a small 4-fold square unit cell within a larger square unit cell.

Data Set F

The sample was prepared with two cycles of sputtering and annealing. The sputtering was performed for both cycles at a pressure of $5.5{\cdot}10^{-10}$ $mbar$ and for a duration of 30 minutes, whereas the annealing was performed at a temperature of $\sim$ 800 K for a duration of 15 minutes. The sample was then transferred to the LEED set-up and the diffraction image presented below in fig. 2.9 was obtained at a bean energy of 54eV.

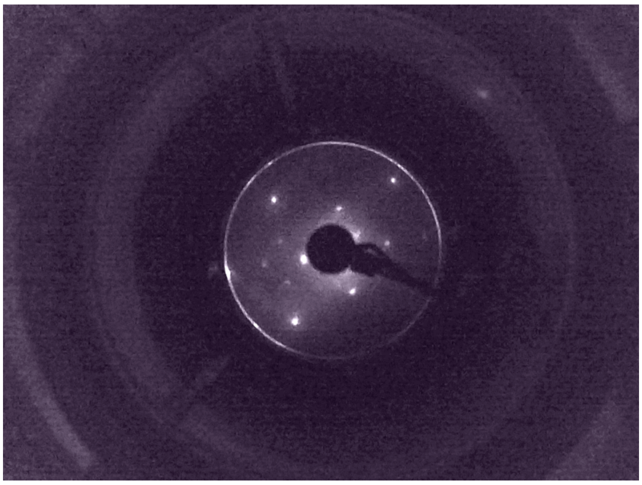

Fig. 2.9: Showing the contrast enhanced LEED data taken of the clean Ni-Al(100) surface, for Data set F.

Congruently to the previous LEED data for the clean Ni-Al(100) surface, a 4-fold square unit cell within a larger square unit cell is observed. It is noted that the camera was zoomed further out from the region of interest with the image presented in fig. 2.9, which was somewhat serendipitous. Unfortunately due to a poorly conducting tip, the STM was unable to achieve any clear images. The tip was later sputtered for use in the next experimental session, as time did not permit for another attempt at scanning on the day.

Data Set G

The sample was subjected to two cycles of sputtering and annealing and then left overnight, whereby in the morning it was then cleaned for a further cycle. The sputtering for all three cycles was performed at a pressure of $5.5 \cdot 10^{-5}$ $mbar$ for a duration of 30 minutes, whereas the annealing was performed at a temperature of $\sim$ 800 K for a duration of 15 minutes with 30 minutes for cooling. After the single cleaning cycle in the morning, the sample was annealed for a further 90 minutes at $\sim$ 600 K to ensure that the surface was not effected by surface segregation of contaminant from the bulk. The pressure remained steady over this period and thus the sample was deemed to be sufficiently clean. Thus after a period of 60 minutes for cooling, the sample was subsequently transferred into the STM chamber, whence the images presented below within fig. 2.10 and fig. 2.11 were obtained.

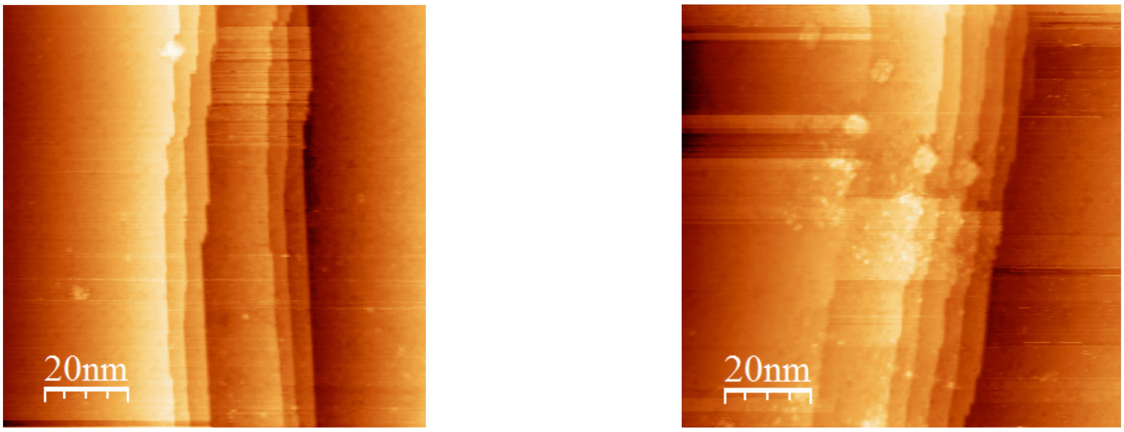

(a) **(b)**

Fig. 2.10: STM data showing terraces of the clean Ni-Al(100) surface, for Data set G.

Interestingly the image presented in fig. 2.10b appears to have identical steps and terraces, which initially would appear somewhat unlikely. Furthermore, comparison with fig. 2.10a would further suggest that such an occurrence may in fact be due to an induced effect of the STM.

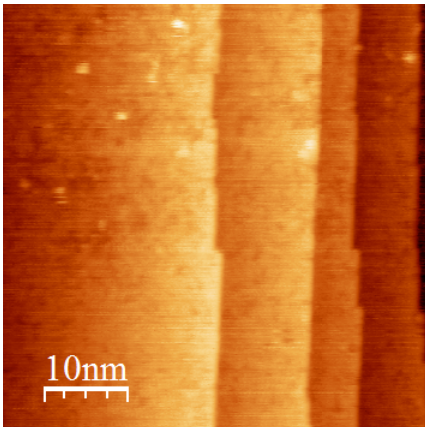

Fig. 2.11: STM data showing terraces of the clean Ni-Al(100) surface, for Data set G.

The image displayed in fig. 2.11 appears to posses no such repeated identical terraces or steps and furthermore displays several clearly defined steps, albeit with some level of noise and surface contaminant also present.

2.3 Investigation of Zn-Pc Deposited Onto the Ni-Al(100) Surface

Over the course of several experimental sessions the evaporation current[5] required for the deposition of Zn-Pc was determined to be[6] 9.6 A, through deposition on the Ag(100) surface which has been shown to successfully form Zn-Pc thin films [28]. Deposition was confirmed via the observation of a LEED pattern.

Data Set H

The initial chamber pressure was $3.9 \cdot 10^{-10}$ $mbar$. The sample was sputtered for 30 minutes at a pressure of $5.5 \cdot 10^{-5}$ $mbar$, after the which the TSP was flushed in order to avoid the absorption of contaminant during subsequent annealing. The sample was then annealed for 15 minutes at a temperature of ~ 800 K, after which it was cooled for 30 minutes. The Zn-Pc was then deposited for 4 minutes at the flux corresponding to 9.6 A applied to the thermal evaporator, after which the TSP was again flushed and the sample was transferred to the STM chamber where the following image was obtained.

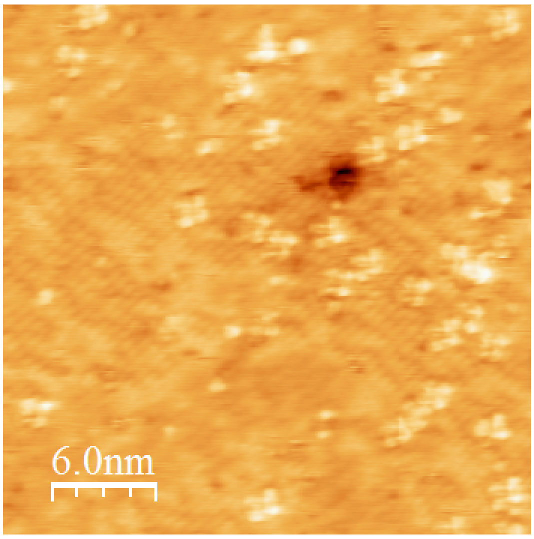

Fig. 2.12: Showing atomic resolution STM data of the Zn-Pc molecule deposited on the Ni-Al(100) surface, for Data set H.

The image doesn't appear visually to suffer from significant noise levels, however the underlying substrate is only displayed very weakly. The molecules lie flat on the surface with most of them seemingly still in-tact. There is also a large surface vacancy in the upper region of the image.

---

[5] To be supplied to the thermal evaporator.

[6] The corresponding temperature was not known as the thermal evaporator had not been characterised.

Data Set I

The sample was sputtered at a pressure of $5.5 \cdot 10^{-5}$ $mbar$ for a duration of 30 minutes and the TSP was subsequently flushed. The sample was then annealed at ~ 800 K for 15 minutes and allowed to cool for 30 minutes. The Zn-Pc was then deposited at a current of 9.6 A for 60 minutes, after which the sample was assessed via LEED. Based on the analysis of the image presented within fig. 2.12, the associated coverage is taken as 0.75 ML (75 % of a single monolayer). The TSP was flushed prior to the LEED being operated in order to prevent the ambient pressure from scattering the electron beam. The LEED beam energy was taken up to 19 eV so as to prevent any fragmentation of the molecule due to the impacting electrons. The subsequent LEED images showed no diffraction pattern, indicating no long range order. Unfortunately no STM images were obtained due to high noise levels, which was indicated by the spectrum analyser within the WSxM^{TM} software to be from an internal source, i.e. from the STM tip or the sample. Moreover, the efforts to remove this noise proved to be in vain, not for a lack of several hours attempt at doing so.

Consequently the molecule was deposited for a further 30 minutes with a current of 9.6 A applied to the thermal evaporator, after which LEED was again utilised to asses the surface. The corresponding coverage was thus $\sim$ 1.13 ML. Unfortunately the LEED data revealed no diffraction pattern once more despite the chamber pressure in the order of 10^{-10} $mbar$. Moreover this deposition and LEED cycle was repeated a further two times resulting in c a coverage of 1.50 ML and 1.88 ML, for each of which no long range order was observed. For sample was annealed for 20 minutes at ~ 400 K for the 1.88 ML coverage before again being assessed by LEED. No subsequent diffraction pattern was observed.

Chapter 3

Analysis And Discussion

The following section is intended to present an analysis of the results and to provide a discussion into what was observed.

3.1 Analysis

3.1.1 Analysis for the Clean Ni-Al(100) Surface

The LEED data presented within data sets B,E and F all displayed similar features and thus in the interest of being concise, the analysis will be relevantly presented with the LEED data handled together as opposed to the chronological ordering that was more suitable for the presentation of the experimental procedure and results.

Data Sets B,E and F

All LEED data taken within data sets B,E and F displayed four possible unit cells. The LEED data taken at 62 eV beam energy from data set E most clearly displays these unit cells, and is replicated below for comparison with a corresponding real space VESTA^{TM} model of the Ni-Al(100) surface in fig. 3.1. It is noted that due to the nature of reciprocal space, the smaller square yellow unit cell within the larger white unit cell as seen in fig. 3.1a corresponds in real space to the reversed arrangement, as is displayed by the colour of the unit cells within the model and the LEED image. Furthermore the shorter (longer) length of the rectangular unit cell in reciprocal space corresponds to the longer (shorter) length of the rectangular unit cell in real space.

Before the lengths of the unit cells could be measured, a scale between the number of pixels between two points in the image and a distance within reciprocal space had to be acquired. The known system used for calibration was the well understood Ag(100) surface, from which a scale of 75.68 Pixels $\AA$

was obtained[1]. Furthermore, before this scale could be applied to the data of interest, two issues regarding scaling between the data of interest and the calibration data had to be resolved.

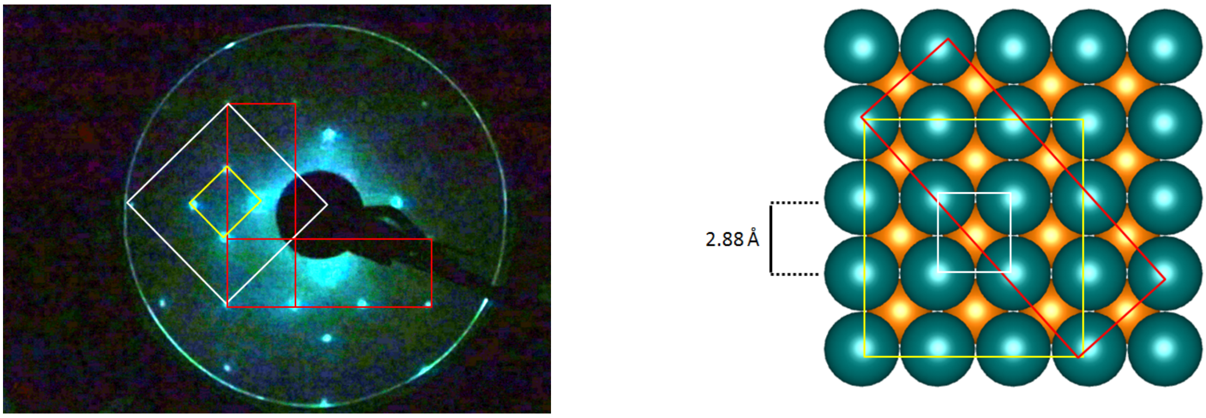

(a) Showing LEED data of the Ni-Al(100) surface taken at 62 eV beam energy.

(b) Showing a VESTA^{TM} model of the NI-Al(100) surface with the observed unit cells.

Fig. 3.1: Showing the contrast enhanced LEED data taken of the clean Ni-Al(100) surface, for Data set E.

The first such issue was due to the image for the calibration data being taken with a different scale of 480x640 pixels whereas the data of interest was taken with an image containing 1200x1600 pixels. Elaborating, the consequence of the mismatch with the number of pixels in an image is that the number of pixels between two points of a fixed physical distance in real space would differ between the two images. This is due to the images within the data of interest essentially having more pixels with which to fill the space between the two points. Fortunately the issue is resolved easily by multiplying the measured lengths in units of pixels[2] by the ratio of the pixels in the images, which is 2/5 for converting between length in the data of interest to that in the calibration data where the calibration scale is valid.

The second issue is that the cameras positioning and zoom setting resulted in the region of interest containing a different number of pixels, leading to a similar discrepancy as with the first issue. Fortunately this issue is rectified by using a common feature within all images of a fixed size, which in this particular case is the diameter of the fluorescent screen which is seen as a clear ring around the area of interest in all images. The correction is performed by measuring diameter for several orientations and obtaining an average in the case of both the calibration data and the data of interest. The value obtained from the calibration data is then divided by that from the data of interest and the resultant value is taken as the correction for the difference in zoom between the two images. The correction is employed by multiplication with the length measured, before using the calibration scale and after having corrected for the first issue. The diameter measurements taken for data sets B,E and F are presented below in table 3.1 whereas those for the calibration data are provided within chapter C. As can be seen from comparison of table 3.1 with table C.2, data sets B and E differed greatest from the calibration data with respect to zoom.

---

[1] The full calibration data and analysis is provided within chapter C.

[2] Specifically, this correction is employed before using the scale between distance in pixels and distance in reciprocal

	Measurement (Pixels)	Repeat 1 (Pixels)	Repeat 2 (Pixels)	Repeat 3 (Pixels)	Average (Pixels)
Data Set B (52eV)	1106.18	1104.09	1104.65	1107.34	1105.57
Data Set E (62eV)	1101.23	1100.59	1100.37	1098.20	1100.10
Data Set E (51eV)	1100.03	1106.18	1102.41	1100.49	1102.28
Data Set F (54eV)	540.09	538.09	536.21	537.67	538.02

Table. 3.1: Showing the measurements of the diameter of fluorescent screen for data sets B,E and F.

The lengths of the white and yellow unit cells as shown within fig. 3.1a were measured and analysis was performed using the two corrections and the calibration scale outlined above. The final conversion for distance in reciprocal to distance in real space was calculated using the relation;

$$a_1 = \frac{2\pi}{a_1^\star} \ , \tag{3.1}$$

where a_1 and $a_1^\star$ are the real and reciprocal space lattice spacings respectively [3]. The results of the analysis are outlined below in table 3.2 and table 3.3 for the white and yellow labelled unit cells respectively[3][4].

	Measurement (Pixels)	Repeat 1 (Pixels)	Repeat 2 (Pixels)	Repeat 3 (Pixels)	Average (Pixels)	Distance ($\mathring{A}$)
Data Set B (52eV)	446.16 ±28	443.52 ±28	444.54 ±28	443.48 ±28	444.43 ±28	2.70 ±0.17
Data Set E (62eV)	387.66 ±28	394.87 ±28	400.42 ±28	394.69 ±28	394.41 ±28	3.03 ±0.22
Data Set E (51eV)	451.16 ±28	450.43 ±28	450.71 ±28	450.07 ±28	450.59 ±28	2.65 ±0.16
Data Set F (54eV)	214.87 ±28	215.15 ±28	216.09 ±28	213.72 ±28	214.96 ±28	2.71 ±0.11

Table. 3.2: Showing the measurements of the white unit cell (w.r.t. fig. 3.1a) for data sets B,E and F.

Employing the consistency check outlined in chapter B and taking the expected value as 2.88±0.01 $\mathring{A}$ from the precision given by the VESTA$^{\text{TM}}$ software, the data sets were found to be consistent with the model value within; two multiples of the experimental error[5] (2σ) for data sets B and F, and to within σ for the images of data set E. The associated errors are within ~ 7 %, indicating that the above consistency values are valid and not simply the product of significantly large uncertainties.

---

space obtained from the calibration data.

[3] A discussion of the error calculation used for the LEED data is presented within chapter B. Note that the error of ±28 pixels is conservative and thus it is taken as the error for the average!

[4] Note that all values to have stated to their measured precision to avoid rounding errors, whereas the final value has been stated to the same precision so as not to skew the range of possible values as dictated by the associated error.

[5] Note that σ is being defined as one multiple of the experimental error.

	Measurement (Pixels)	Repeat 1 (Pixels)	Repeat 2 (Pixels)	Repeat 3 (Pixels)	Average (Pixels)	Distance ($\AA$)
Data Set B (52eV)	141.45 ±28	143.18 ±28	144.80 ±28	147.85 ±28	144.32 ±28	8.31 ±1.16
Data Set E (62eV)	140.19 ±28	142.84 ±28	130.11 ±28	135.70 ±28	137.21 ±28	8.69 ±1.78
Data Set E (51eV)	138.59 ±28	145.67 ±28	145.73 ±28	148.55 ±28	144.64 ±28	8.26 ±1.60
Data Set F (54eV)	72.69 ±28	71.27 ±28	70.26 ±28	73.69 ±28	71.98 ±28	8.10 ±0.95

Table. 3.3: Showing the measurements of the yellow unit cell (w.r.t. fig. 3.1a) for data sets B,E and F.

Employing the consistency check once more and taking the expected value as $8.64 \pm 0.01\ \AA$ based on the VESTA$^{\text{TM}}$ model shown in fig. 3.1b, the sets were all found to be consistent with the model to within σ. However it is noted that the error for the yellow unit cell is considerably larger ($\sim 20\ \%$)than for the white unit cell, which is a consequence of a smaller size in reciprocal space and thus a larger percentage error based on the set initial error taken for a length measurement of ±28 pixels[6].

Unfortunately eq. (3.1) does not provide a valid scaling between real space and reciprocal space when the lattice vectors are not the bravais lattice vectors. This can be proven with the simple case of a right-angled triangle with unit length sides which are themselves taken as in the direction of the bravais lattice vectors and thus for which eq. (3.1) is valid. The corresponding hypotenuse from pythagoras theorem is;

$$\begin{aligned} h = &\ \sqrt{1^2 + 1^2}\ , \\ = &\ \sqrt{2}\ . \end{aligned}$$

Converting this distance from reciprocal space to real space directly using eq. (3.1);

$$\begin{aligned} h' = &\ \frac{2\pi}{h}\ , \\ = &\ \frac{2\pi}{\sqrt{2}}\ , \end{aligned}$$

whereas if the components are converted individually before applying pythagoras' theorem;

$$\begin{aligned} h' = &\ \sqrt{\left(\frac{2\pi}{1}\right)^2 + \left(\frac{2\pi}{1}\right)^2}\ , \\ = &\ \frac{4\pi}{\sqrt{2}}\ . \end{aligned}$$

Thus converting the hypotenuse of a right-angled triangle with equal length sides which are in the

---

[6] Please see chapter B for clarification. The initial error is taken as ±28 pixels, however the error will propagate differently for each measurement.

direction of the bravais lattice vectors requires an alteration to eq. (3.1). The appropriate relation in this case, as shown above is given by;

$$h = \frac{4\pi}{h^{\star}} \ , \tag{3.2}$$

where h and $h^{\star}$ are the real and reciprocal space distances respectively[7]. As a sanity check, fig. 3.1a supports that the short length of the red unit cell should equal the diagonal of the yellow unit cell, as measured in reciprocal space. The raw data indeed supports this observation, however the associated longer length of the red unit cell does not equal the diagonal of the yellow unit cell in real space when translating with eq. (3.1). Moreover the two square unit cells do in-fact convert to real space in the anticipated manner, maintaining yet reversing their relative size of 1/3. Elaborating, this suggests that the unit cells posses a given relative size in reciprocal space that is not translated in the expected way into real space when using eq. (3.1), despite the square unit cells translating in the expected manner. Thus the translation of the red unit cell would appear to be where the anomaly exists, as supported by the simple example above. Thus the lengths of the rectangular unit cell was measured, the results for which are presented below[8] in table 3.4 and table 3.5.

	Measurement (Pixels)	Repeat 1 (Pixels)	Repeat 2 (Pixels)	Repeat 3 (Pixels)	Average (Pixels)	Distance ($\mathring{A}$)
Data Set B (52eV)	211.03 ±28	202.00 ±28	205.07 ±28	210.96 ±28	207.27 ±28	11.57 ±3.13
Data Set E (62eV)	194.00 ±28	194.99 ±28	202.00 ±28	193.01 ±28	196.00 ±28	12.17 ±3.48
Data Set E (51eV)	204.01 ±28	201.60 ±28	203.73 ±28	204.98 ±28	203.58 ±28	11.74 ±3.23

Table. 3.4: Showing the measurements of the short length of the red unit cell (w.r.t. fig. 3.1a) for data sets B and E.

The expected value for the shorter (in reciprocal space) length of the rectangular unit cell[9] as given by fig. 3.1b is 12.22 ± 0.01 $\mathring{A}$ with the error again taken from the precision of the VESTA$^{\text{TM}}$ software. Consequently the all three sets of data display consistency with the model to within σ, however it is noted that as with the yellow unit cell the error is considerably large at ~ 25 % as a result of the small length in reciprocal space. Reiterating, the uncertainty in the measurement is $\sim \pm 20$ pixels at each point of measurement, corresponding to an uncertainty in length of ±28 pixels as discussed in chapter B. This fixed initial error with result in a larger percentage error for smaller length measurements.

---

[7] There is no reference for this, it was simply figured out after the observations for the square unit cells supported the model in fig. 3.1b whereas the rectangular unit cell had dimensions of half the expected values.

[8] The LEED image from data set F did not display the diffraction spots required to assess the rectangular unit cell.

[9] Remembering that the shorter length in reciprocal space corresponds to the longer length in real space.

	Measurement (Pixels)	Repeat 1 (Pixels)	Repeat 2 (Pixels)	Repeat 3 (Pixels)	Average (Pixels)	Distance (Å)
Data Set B (52eV)	636.96 ±28	630.66 ±28	631.02 ±28	635.78 ±28	633.61 ±28	3.78 ±0.33
Data Set E (62eV)	582.17 ±28	586.00 ±28	586.00 ±28	570.01 ±28	581.05 ±28	4.11 ±0.40
Data Set E (51eV)	646.00 ±28	632.00 ±28	638.45 ±28	637.55 ±28	638.50 ±28	3.74 ±0.33

Table. 3.5: Showing the measurements of the long length of the red unit cell (w.r.t. fig. 3.1a) for data sets B and E.

The expected value for the longer (in reciprocal space) length of the rectangular unit cell as given by fig. 3.1b is 4.07 ± 0.01 $\mathring{A}$ with the error again taken from the precision of the VESTA$^{\mathrm{TM}}$ software. Consequently the all three sets of data display consistency with the model to within σ, which in this case is more significant as the error is only $5 - 10$ %.

Data Set A

The image presented within fig. 2.4a displayed horizontal noise features due to a change in tip conductivity which was a consequence of the tip picking up and dropping contaminating atoms. The colour distribution throughout the terraces also suggests that the sample was not flat during the scan. The raw image was manipulated using the WSxM$^{\mathrm{TM}}$ software to reduce the noise features and account for the samples tilting during the scan via a line by line flattening process followed by a local plane process using the third terrace from the bottom[10]. The resultant image is given below in fig. 3.2a and indeed displays less pronounced noise features and steps which are far more distinguishable and of uniform height. The corresponding height profile for the path displayed as a blue line in fig. 3.2a is presented in fig. 3.2b.

---

[10] These image processing procedures are explained in detail within chapter A.

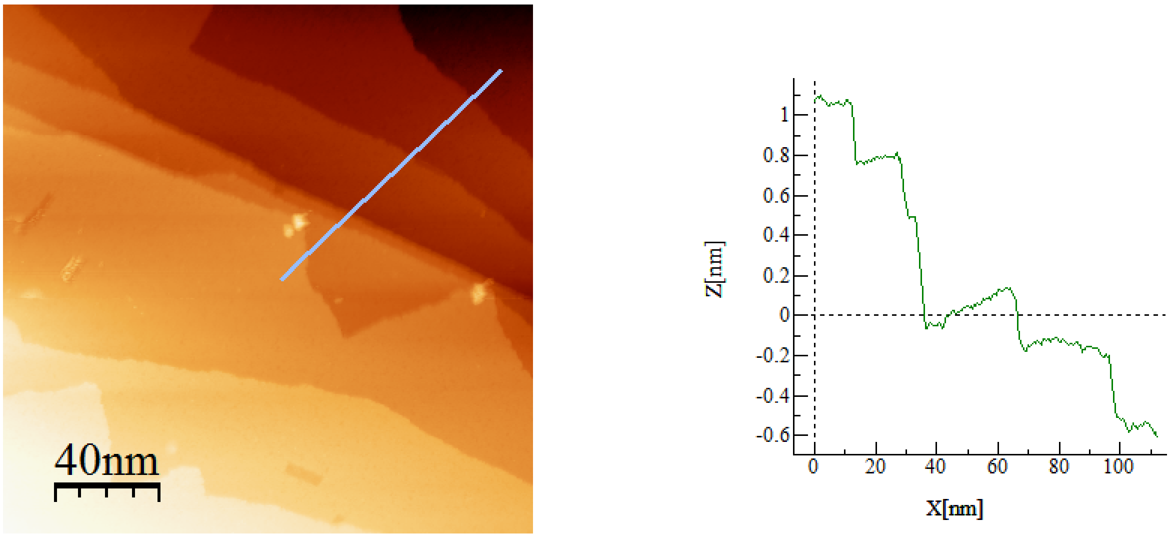

(a) Manipulation of the raw image via flattening and local plane procedures.

(b) Height profile corresponding to the blue line in fig. 3.2a.

Fig. 3.2: STM data showing terraces of the clean Ni-Al(100) surface, for Data set A.

The height profile displays five steps, the second of which is not strongly pronounced. The fourth terrace in particular shows sample tilting which unfortunately could not be removed through image processing without more significant detrimental effects on the other terraces and steps. Consequently the measurements involving this terrace were taken using its midpoint as the true height of the terrace. The step heights as measured from the profile in fig. 3.2b were measured, the results of which are presented below in table 3.6.

	Measurement (*nm*)	Repeat 1 (*nm*)	Repeat 2 (*nm*)	Average (*nm*)	As a percentage of 0.288 *nm*
Step 1	0.275 ± 0.041	0.274 ± 0.041	0.271 ± 0.041	0.273 ± 0.024	95 ± 8
Step 2	0.296 ± 0.044	0.300 ± 0.045	0.296 ± 0.044	0.297 ± 0.026	103 ± 9
Step 3	0.576 ± 0.086	0.543 ± 0.081	0.541 ± 0.081	0.553 ± 0.048	192 ± 17
Step 4	0.274 ± 0.041	0.283 ± 0.042	0.276 ± 0.041	0.278 ± 0.024	97 ± 8
Step 5	0.399 ± 0.060	0.336 ± 0.050	0.390 ± 0.059	0.375 ± 0.033	130 ± 11

Table. 3.6: Showing the measurements of the step heights relating to the profile displayed within fig. 3.2b.

Any errors for individual measurements[11] and final results presented within this work are discussed within chapter B. As can be seen from table 3.6 above and fig. 1.2, four of the five steps are consistent within the experimental error, with steps between single species. The data for step 5 is only consistent with steps between single species to within 3σ, whereas it is consistent to within 2σ with a combination of both a step between single species and a step between the species, i.e. a step of 2.88 $\AA$ between Al layers and a subsequent step of 1.44 $\AA$ between an Al and a Ni layer. This step is associated to the right most step in fig. 3.2a. Moreover, during image processing it was not possible to display all terraces as being individually flat, and thus the lower terrace of step 5 which is associ-

---

[11] In the case of STM data the errors are taken from percentages of the measured value, and then propagated as outlined in chapter B.

ated with the right most terrace in fig. 3.2a was only partially profiled due to noise. Furthermore, it would thus not be possible to determine whether the terrace experienced a noise feature at the foot of the step and hence it is not clear as to whether the measurement in step 5 is entirely valid.

Furthermore the image presented within fig. 2.4b displayed high levels of noise and nonuniform terraces and thus a line by line flattening procedure was employed, the resultant image of which is given below in fig. 3.3 alongside the corresponding height profile.

(a) Manipulation of the raw image via a flattening procedure.

(b) Height profile corresponding to the blue line in fig. 3.3a.

Fig. 3.3: STM data showing a surface vacancy of the clean Ni-Al(100) surface, for Data set A.

The corresponding depth measurements[12] for the vacancy are presented below in table 3.7.

	Measurement (Å)	Repeat 1 (Å)	Repeat 2 (Å)	Average (Å)	As a percentage of 2.88 Å
Depth	1.395 ± 0.209	1.393 ± 0.209	1.381 ± 0.207	1.390 ± 0.120	48 ± 4

Table. 3.7: Showing the measurements of the vacancy depth relating to the profile displayed within fig. 3.2b.

Interestingly the surface vacancy is only a single layer deep, as the depth measured corresponds to the interlayer spacing as shown within fig. 1.2.

Additionally, the atomic resolution image presented within fig. 2.3b displayed a wavy pattern within its upper half. Unfortunately the height profiles of the raw image and a flattened image displayed considerable noise and were thus unusable. However an FFT was taken[13] of the raw image, enabling a height profile to be taken of the subsequent IFFT. The FFT and corresponding IFFT are presented below within fig. 3.5.

---

[12] Note that the measured values are stated to the precision of the software for completeness of information, as the errors are taken as a percentage of the measured value and moreover doing otherwise would skew the range of possible values permitted by the error. It is left to the capable reader to determine the significance of the measurements.

[13] A full discussion of STM image processing is provided within chapter A.

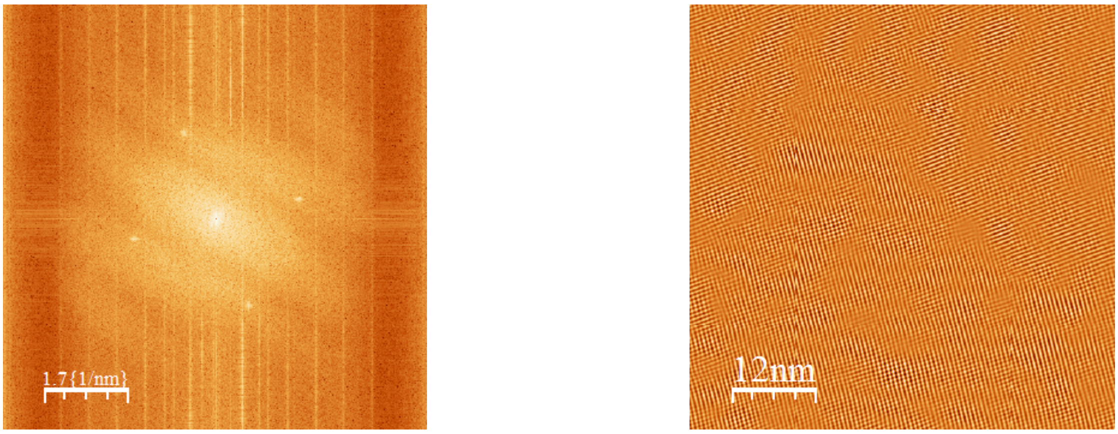

(a) Showing an FFT taken with the image from fig. 2.3b.

(b) Showing the IFFT corresponding to the 4 spots within fig. 3.4a.

Fig. 3.4: Showing an FFT and IFFT taken using fig. 2.3b.

Evidently from fig. 3.4a the surface possess a 4-fold unit cell and furthermore we see considerable background noise for the periodicity. The periodicity of the unit cell for the ordered lower region of the image was measured in each principle axis (Axis 1 and Axis 2) as presented below[14] in table 3.8. Furthermore a long range periodicity was observed, and is also presented in the table below within the row titled 'feature L'.

	Measurement (nm)	Repeat 1 (nm)	Repeat 2 (nm)	Average (nm)
Axis 1	0.626 ± 0.125	0.593 ± 0.119	0.626 ± 0.125	0.615 ± 0.071
Axis 2	0.534 ± 0.107	0.534 ± 0.107	0.563 ± 0.113	0.544 ± 0.063
feature L	3.759 ± 0.752	3.614 ± 0.723	3.759 ± 0.752	3.542 ± 0.429

Table. 3.8: Showing the measurements of the periodicity of the principle unit cell and the long range oscillation as seen in fig. 3.4b.

The results for the unit cell as denoted by Axis 1 and Axis 2 are only consistent with the expected unit cell dimensions of 0.288 ± 0.001 nm to within 5σ. However the horizontal error estimated for the set-up did not account for the observed wavy nature of the image. Consequently if the wavy nature is indeed associated with a standing wave produced by friedel oscillations as outlined within chapter 1, then the error may in-fact be a gross underestimation. Moreover the measurements of the unit cell using this data can not be confirmed to be valid, as the interference effects contributing to the results are neither quantified or understood. Furthermore, the result of the most interest is the longer range periodicity of 3.5 ± 0.4 nm which may relate to the wavelength of the potential long range standing wave, induced by friedel oscillations around point defects on the surface. Unfortunately the visual standing wave cannot be simply associated with a friedel oscillation as it does not appear as a prototypical friedel oscillation around a single point defect. The structure of the wavy pattern may in-fact result from the superposition of friedel oscillations induced by scattering at multiple

---

[14] Note that the error is taken as 20 % of the measured value as outlined within chapter B, thus for completeness the values measured are stated to their full precision as measured by the software, for the sake of reproducibility!

point defects on the surface. Moreover, despite the observation being far from conclusive regarding the occurrence of friedel oscillations on the Ni-Al(100) surface, the observation of the wavy image within fig. 2.3b and the long range periodicity denoted by feature L must nonetheless be noted and considered in the context of further investigation.

Additionally the height profiles used to measure the periodicity in the principle unit cell (for Axis 1) and that of the longer range feature are presented within fig. 3.5a and fig. 3.5b respectively.

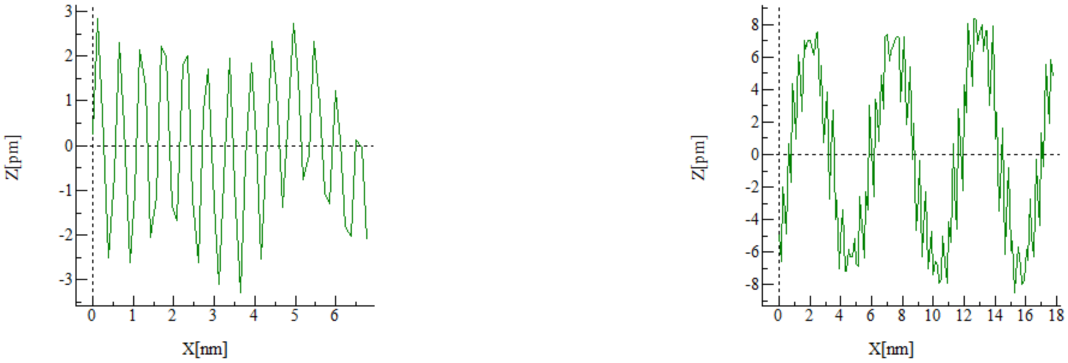

(a) Showing the height profile for the orientation denoted as Axis 1 of table 3.8.

(b) Showing the height profile of the oscillation denoted as feature L of table 3.8.

Fig. 3.5: Showing an FFT and IFFT taken using fig. 2.3b.

Data Set C

The image presented in fig. 2.6 displayed a considerable artifact running horizontally across it's centre and moreover had terraces of individually nonuniform height[15]. Subsequently the image was improved using a local place procedure on the upper most terrace. The resultant image and corresponding height profile are presented below in fig. 3.6.

---

[15] The significance of this issue is highlighted explicitly within chapter A.

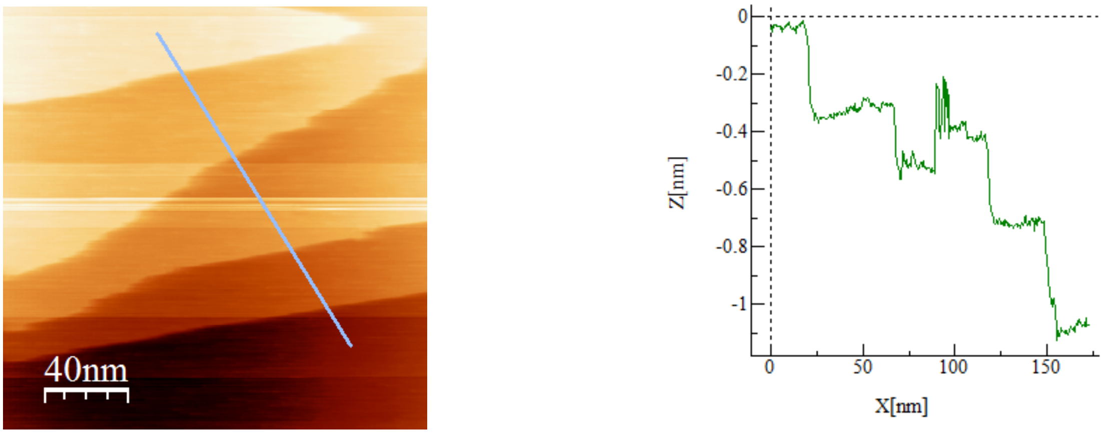

(a) Manipulation of the raw image via a local plane procedure.

(b) Height profile corresponding to the blue line in fig. 3.6a.

Fig. 3.6: STM data showing terraces of the clean Ni-Al(100) surface, for Data set C.

The height profile was taken over the path with the least noise and most clearly defined steps, however the second step (from the left) has a significant noise feature running through it as seen in fig. 3.6b and was thus unusable. Furthermore the final step also experienced a noise feature and upon investigation was found to be masked by a large pseudo-step. The true lower terrace of the lower step can be seen in fig. 3.6b as a minor protrusion from the final step at approximately two thirds of the way down. The corresponding height measurements[16] are presented below in table 3.9.

	Measurement (*nm*)	Repeat 1 (*nm*)	Repeat 2 (*nm*)	Average (*nm*)	As a percentage of 0.288 *nm*
Step 1	0.279 ± 0.042	0.303 ± 0.045	0.261 ± 0.039	0.281 ± 0.024	98 ± 8
Step 3	0.295 ± 0.044	0.323 ± 0.048	0.298 ± 0.045	0.305 ± 0.026	106 ± 9
Step 4	0.262 ± 0.039	0.265 ± 0.040	0.285 ± 0.043	0.271 ± 0.023	94 ± 8

Table. 3.9: Showing the measurements of the step heights relating to the profile displayed within fig. 3.6b.

The results in table 3.9 display three steps which agree with a step size of 2.88 ± 0.01 $\AA$ to within σ.

Data Set D

The image presented in fig. 2.7 displayed significant noise features which were removed during subsequent image processing by implementing a line by line flattening procedure and a subsequent local plane procedure on the right most terrace. The resultant image and corresponding height profile are presented below in fig. 3.7.

---

[16] Once more the errors are taken as a percentage of the measured value, as outlined in chapter B.

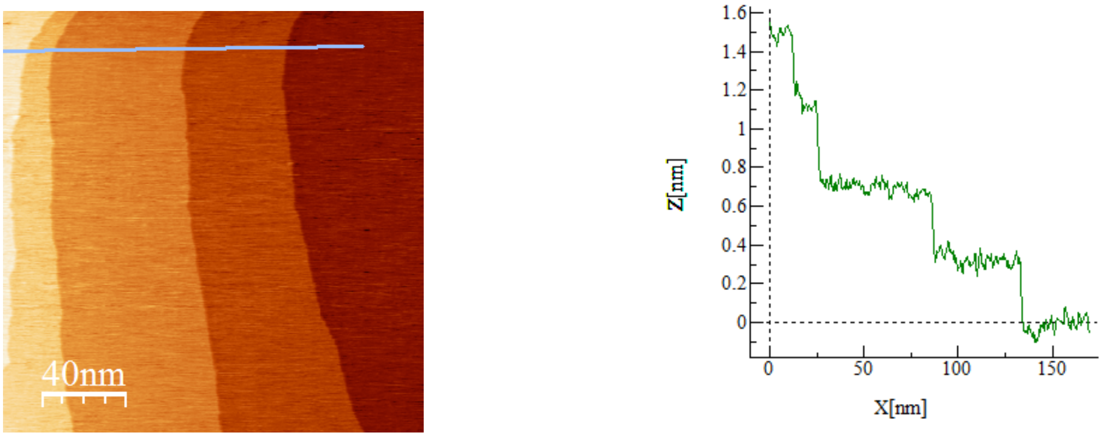

(a) Manipulation of the raw image via flattening and local plane procedures.

(b) Height profile corresponding to the blue line in fig. 3.7a.

Fig. 3.7: STM data showing terraces of the clean Ni-Al(100) surface, for Data set D.

Both fig. 3.7a and fig. 3.7b display unform terraces with clearly distinguished steps, the measurements for which are presented below within table 3.10.

	Measurement (*nm*)	Repeat 1 (*nm*)	Repeat 2 (*nm*)	Average (*nm*)	As a percentage of 0.288 *nm*
Step 1	0.365 ± 0.055	0.313 ± 0.047	0.335 ± 0.050	0.338 ± 0.029	117 ± 10
Step 2	0.379 ± 0.057	0.371 ± 0.056	0.444 ± 0.067	0.398 ± 0.035	138 ± 12
Step 3	0.340 ± 0.051	0.373 ± 0.056	0.353 ± 0.053	0.355 ± 0.031	123 ± 11
Step 4	0.341 ± 0.051	0.332 ± 0.050	0.292 ± 0.044	0.322 ± 0.028	112 ± 10

Table. 3.10: Showing the measurements of the step heights relating to the profile displayed within fig. 3.7b.

Interestingly, of the four steps in table 3.10 only two display consistency with a single step of 2.88 ± 0.01 $\mathring{A}$ to within 1σ, whereas the other two steps are either equally consistent or more consistent with a single 2.88 ± 0.01 $\mathring{A}$ step on top of an immediate half[17] step of 1.44 ± 0.01 $\mathring{A}$. Unlike with the similar observation from step 5 of data set A, there exists no significant variation of height within any individual terrace, suggesting that the observation may be valid evidence of steps between terraces[18] of Ni and Al. It is however possible that the steps are between terraces of like species[19], considering that the two questionable steps are not considerably bias toward either interpretation.

Data Set G

The image presented within fig. 2.10b displayed an apparent set of identical features on neighbouring terraces. The image was corrected for noise via a line by line flattening procedure, after which a

---

[17] Based on defining a single step as being ~ 2.88 $\mathring{A}$ tall for simplicity.

[18] In an ideal sample these layers would be purely composed of either Ni or Al, however in practice they may contain antisites of the opposite species (see chapter 1) [18].

[19] Which according to literature would be energetically preferable to be Al terraces (see chapter 1) [17].

local plane procedure using the right most terrace was employed to correct for sample tilting during the scan. The resultant image and corresponding height profile are displayed below within fig. 3.8.

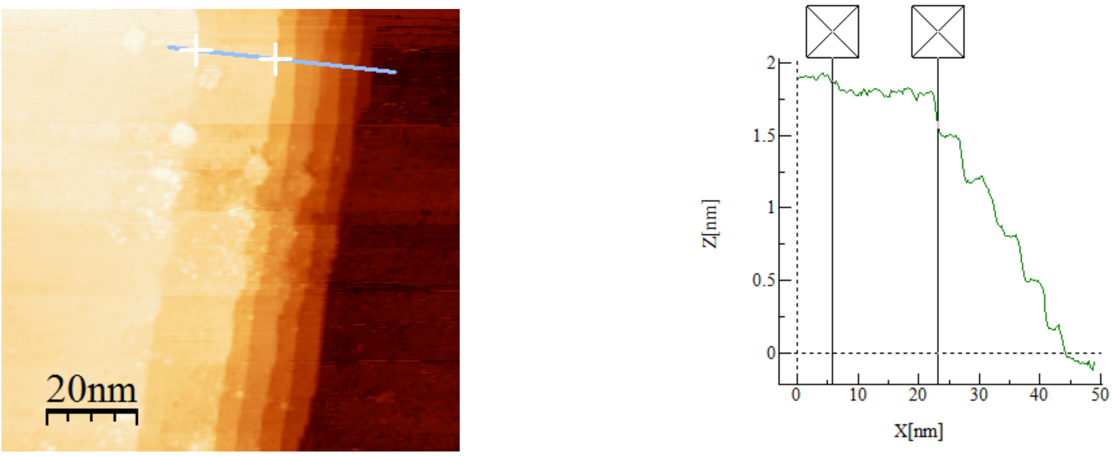

(a) Manipulation of the raw image via flattening and local plane procedures.

(b) Height profile corresponding to the blue line in fig. 3.8a.

Fig. 3.8: STM data showing terraces of the clean Ni-Al(100) surface, for Data set G.

Interestingly the profile displayed in fig. 3.8b identifies the left identical step as a pseudo-step and the central identical step as a genuine step. Thus it can be concluded that this feature was a consequence of an effect experienced by the STM tip. Moreover this is a common occurrence within STM scans which is an effect induced by the tip having multiple end-points and in the present case there would seemingly be three such end-points as indicated by the three identical terraces.

Furthermore the images in fig. 2.10a and fig. 2.11 also displayed noise and nonuniform terraces. Subsequently they were each subjected to a line by line flattening procedure and a local plane procedure. The resultant image from the raw data displayed in fig. 2.10a is presented below in fig. 3.9 alongside the corresponding height profile.

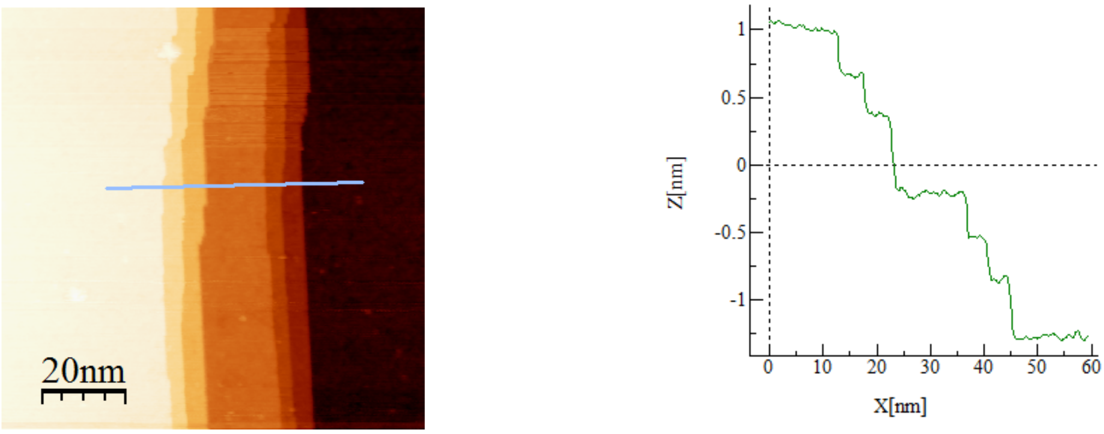

(a) Manipulation of the raw image via flattening and local plane procedures.

(b) Height profile corresponding to the blue line in fig. 3.9a.

Fig. 3.9: STM data showing terraces of the clean Ni-Al(100) surface, for Data set G.

Both the image and profile displayed in fig. 3.9 reveal uniform terraces with low noise levels and clearly defined steps. The associated height measurements are presented below in table 3.11.

	Measurement (*nm*)	Repeat 1 (*nm*)	Repeat 2 (*nm*)	Average (*nm*)	As a percentage of 0.288 *nm*
Step 1	0.336 ± 0.050	0.321 ± 0.048	0.334 ± 0.050	0.330 ± 0.028	115 ± 10
Step 2	0.267 ± 0.040	0.288 ± 0.043	0.284 ± 0.043	0.280 ± 0.024	97 ± 8
Step 3	0.592 ± 0.089	0.610 ± 0.092	0.548 ± 0.082	0.583 ± 0.051	202 ± 18
Step 4	0.320 ± 0.048	0.294 ± 0.044	0.323 ± 0.048	0.312 ± 0.027	108 ± 9
Step 5	0.342 ± 0.051	0.320 ± 0.048	0.329 ± 0.049	0.330 ± 0.028	115 ± 10
Step 6	0.437 ± 0.066	0.422 ± 0.063	0.444 ± 0.067	0.434 ± 0.038	151 ± 13

Table. 3.11: Showing the measurements of the step heights relating to the profile displayed within fig. 3.9b.

The results displayed within table 3.11 are composed of; two steps that agree with the single step value of 2.88 ± 0.01 $\mathring{A}$ to within σ and a further two steps that agree to within 2σ, an individual step that agrees with the double step value of 5.76 ± 0.01 $\mathring{A}$ to within σ and perhaps more interestingly an individual step that agrees with a combination of a single step and a half step of 1.44 ± 0.01 $\mathring{A}$ to within σ.

The processed image from the data in fig. 2.11 and the corresponding height profile are presented below in fig. 3.10.

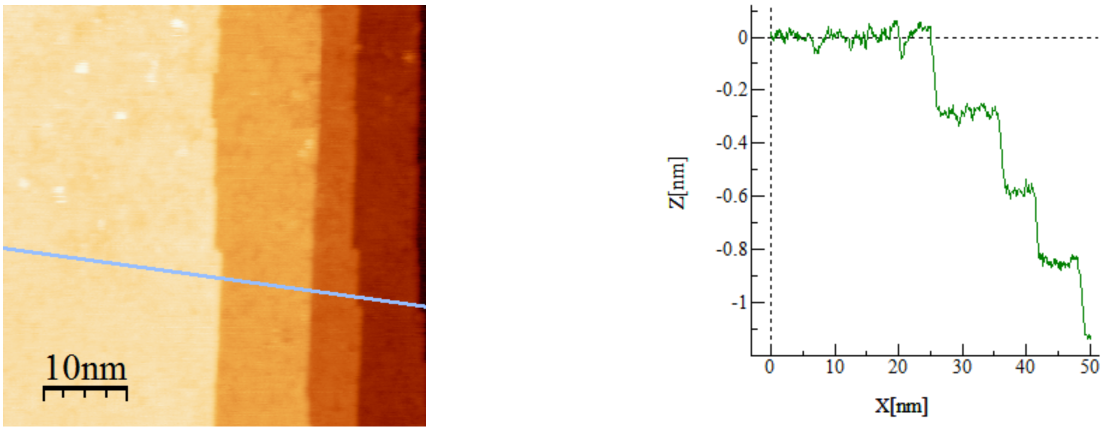

(a) Manipulation of the raw image via flattening and local plane procedures.

(b) Height profile corresponding to the blue line in fig. 3.10a.

Fig. 3.10: STM data showing terraces of the clean Ni-Al(100) surface, for Data set G.

The image and profile presented in fig. 3.10 display four well defined steps with the two upper terraces experiencing considerable noise which is potentially the result on contaminant as displayed in fig. 3.10a. The corresponding measurements are summarised below in table 3.12.

	Measurement (*nm*)	Repeat 1 (*nm*)	Repeat 2 (*nm*)	Average (*nm*)	As a percentage of 0.288 *nm*
Step 1	0.294 ± 0.044	0.304 ± 0.046	0.315 ± 0.047	0.304 ± 0.026	106 ± 9
Step 2	0.282 ± 0.042	0.293 ± 0.044	0.301 ± 0.045	0.292 ± 0.025	101 ± 9
Step 3	0.279 ± 0.042	0.269 ± 0.040	0.279 ± 0.042	0.276 ± 0.024	96 ± 8
Step 4	0.294 ± 0.044	0.283 ± 0.042	0.289 ± 0.043	0.289 ± 0.025	100 ± 9

Table. 3.12: Showing the measurements of the step heights relating to the profile displayed within fig. 3.10b.

The results presented within table 3.12 display four steps, all of which correspond to a single step of height 2.88 ± 0.01 $\mathring{A}$ to within σ.

3.1.2 Analysis for Zn-Pc Deposited Onto the Ni-Al(100) Surface

Data Set H

As is evident from fig. 2.12, the majority of the molecules are orientated to be flat with respect to the substrate, indicating that there is an energetic advantage to exposing the maximum area to the substrate. This may be a result of the significant role of van der walls forces on the interaction between the Zn-Pc molecules and the Ni-Al(100) substrate, which scale with surface area. These observations reveal a different trend than for the Ag(100) system that was used for obtaining deposition conditions, for which it is reported that half of the molecules are orientated stood up [28]. Taking the dimensions of 2.45 ± 0.01 *nm* for the Zn-Pc molecule from fig. 1.1a, the coverage was determined[20] to be ~ 5 %. Furthermore it is apparent that the molecules take two preferential orientations of alignment with the substrate in the plane of the surface, with 40 % aligning one way and 60 % aligning the other[21]. However the molecules do not display an apparent long range ordering at the presented coverage.

Moreover it can be seen that there are various fragments of the Zn-Pc molecule scattered across the surface, indicating fragmentation upon impact of the molecule during deposition. The frequency of such fragmentation is estimated at ~ 11 % based on a total of 4 fragmented molecules distributed over the image. Unfortunately the substrate periodicity could not be measured due to high levels of noise and a low intensity for the substrate atoms within the image.

Data Set I

Due to the lack of data for the experimental session denoted by data set I, all relevant discussion was presented within the above results section.

---

[20] The coverage was calculated using the total area of the surface covered by the Zn-Pc molecules within the image.

[21] These numbers only account for the molecules that are in-tact, and not those that have fragmented.

3.2 Discussion

3.2.1 Discussion of the Clean Ni-Al(100) Surface

The LEED data from data sets B, E and F all support the real space model presented in fig. 3.1b to within σ for the rectangular (red) and larger square (white) reciprocal space unit cells and to within either σ or 2σ for the smaller (yellow) unit cell. It is noted however that the observations for the longer orientation of the rectangular unit cell and the larger white unit cell as observed in reciprocal space and displayed in fig. 3.1a, hold more significant bearing as they possess a smaller percentage uncertainty. Consequently the real space structure is determined to have a p(3 x 3) reconstruction when prepared by annealing at $\sim 800\ K$, or equivalently c($\sqrt{2}$ x 3$\sqrt{2}$)R45° and c(3$\sqrt{2}$ x $\sqrt{2}$)R45° domains, in agreement with the literature as outlined in section 1.1.2.

Furthermore it is claimed that the larger p(3 x 3) unit cell contains within it a p(1 x 1) unit cell directly at it's centre, as indicated by fig. 3.1a and supported by table 3.3 and table 3.2. Moreover it is reported that the Ni-Al(100) surface has a composition of 2/3 Al and 1/3 Ni, distributed within a diagonal row arrangement as shown below in fig. 3.11a.

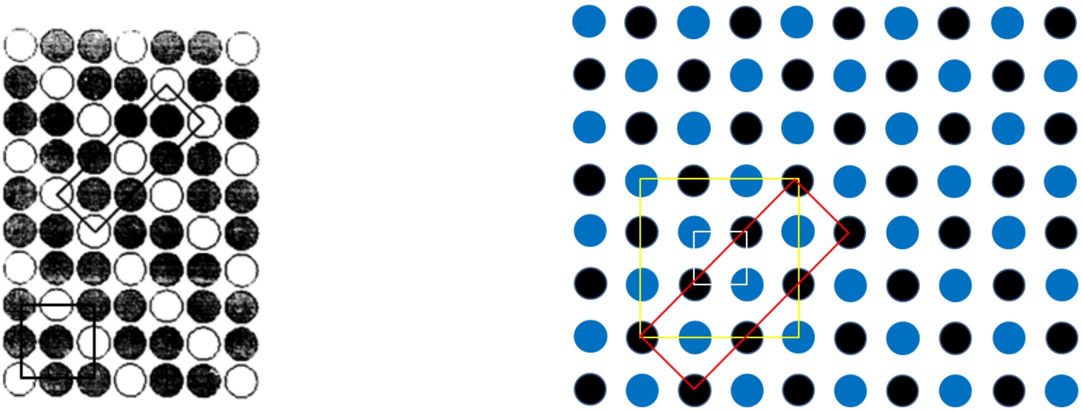

(a) Model from the literature displaying a p(2 x 2) unit cell [29]. Al are black and Ni are white.

(b) Model describing the results, displaying a p(1 x 1) unit cell (white) within a p(3 x 3) unit cell (yellow).

Fig. 3.11: Showing models of the Ni-Al(100) surface for various compositions.

Interestingly, in contradiction to the literature the results presented within this work indicate a surface structure of equal parts Ni and Al, as displayed within fig. 3.11b. Elaborating, the results within table 3.3 clearly support the p(3 x 3) unit cell whereas those within table 3.2 support a p(1 x 1) unit cell. The model in fig. 3.11a would indeed allow for a p(1 x 1) unit cell within the larger 4-fold unit cell and furthermore the positions of the atoms within the smaller unit cell would be positioned at 1/3 and 2/3 of the length of the larger unit cell with the centre of each unit cell directly overlapping. Moreover, due to the relative positioning the smaller unit cell would thus be due to contributions of diffraction from the underlying layer as opposed to the larger unit cell which is a feature of the surface layer. However it would thus be expected that the diffraction spots of the larger unit cell in reciprocal space, corresponding to the smaller unit cell in real space would be less intense than those of the smaller reciprocal space unit cell. This is supported within fig. 2.8b whereas divergent observation are shown within fig. 2.8a. Beams of increasing energy beyond the value of ~ 50 eV implemented within LEED provide measurements that are less surface sensitive, as shown in fig. 1.7 of chapter 1. Consequently the expectation would be for the reverse change in relative intensity of the spots than that which is observed. However this is certainly not conclusive evidence that the model presented within fig. 3.11a should be dismissed.

Unfortunately, the model then fails due to the observation that the larger unit cell has dimensions corresponding to a p(3 x 3) unit cell, for which the only central p(1 x 1) unit cell possible which sits in the required relative position must be that belonging to the surface. Consequently it is claimed that as indicated by the model presented in fig. 3.11b, the only possible surface configuration that can result in the observed diffraction pattern with the determined dimensions, is a configuration of equal parts Ni and Al distributed in a diagonal row arrangement. The disparity between the reported surface composition and that indicated by the results presented, is possibly a consequence of the samples used within the two investigations possessing a different bulk composition, considering that the preparation conditions employed were similar.

Furthermore the ideally terminated Ni-Al(100) surface has been reported[22] to have an energetic preference to Al terminated layers for preparation conditions utilising annealing below 1400 K [29]. Consequently the Ni-Al(100) surface investigated would appear to contain half Al and half Ni antisites. Interestingly an additional observation of importance is that despite this mixture of species within the surface, all height profiles display no surface rippling as reported for the (110) and (111) surfaces. This is suspected to be a consequence of the (110) and (111) planes possessing subsurface layers of mixed Al and Ni, whereas the (100) plane possing subsurface layers of pure[23] Al or Ni.

The STM data from data set A displayed single and double steps with a potential half step superimposed with a single step. This possible half step was however dismissed due to potential noise features at the foot of the corresponding step within the height profile. Nonetheless, valid observations of potential half steps (i.e. steps of 1.44 ± 0.01 $\mathring{A}$) were made within data set D and a further definitive half step was observed within data set G. Consequently, excluding the half step of data set A it is concluded that single steps of 2.88 ± 0.01 $\mathring{A}$ account for 76 % of the steps observed, double steps of 5.76 ± 0.01 $\mathring{A}$ account for a further 10 % whereas the remaining 14 % are accounted for by half steps of 1.44 ± 0.01 $\mathring{A}$. Moreover, 86 % of steps observed were between terraces of like species, whereas 14 % were between terraces of different species[24].

Furthermore, the image presented within fig. 2.4a displayed terraces with 90 degree edges for which the underlying cause was discussed within section 1.5. Moreover, the (100) surface of a BCC structure forms kinks at step edges in the arrangement depicted below within fig. 3.12.

---

[22] Refer to section 1.1.2.

[23] For an ideal bulk termination with no defects.

[24] Assuming that each step is ideally bulk terminated, which in practice is not the case, as supported by the LEED data and within the literature [29].

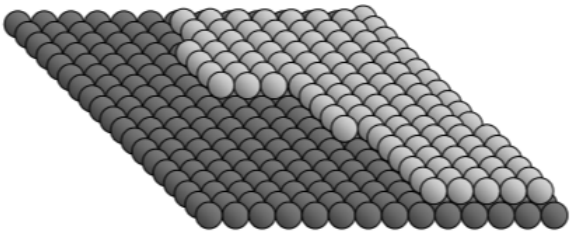

Fig. 3.12: Showing the prototypical form of kinks at the edge of a BCC (100) surface [3].

Elaborating, any kink on the surface offers diffusing adatoms a site of higher coordination number and thus an opportunity to minimise the surface free energy. Furthermore the highest coordination number is achieved by diffusing onto an existing row as opposed to beginning a new row. Consequently the edges of terraces are typically formed by complete rows. However it is possible for adatoms to diffuse to a step edge and before diffusing to a kink site, becoming the site for further adatoms to diffuse to and thus forming a new row. Subsequently the underlying cause of the smooth edged terraces with 90 degree large kinks can be understood. Furthermore fig. 2.4a also displayed surface contaminant which had been pinned to the edges of the third terrace up. This clustering is a consequence of adatoms diffusing along the terrace edge and incidently bonding with one another as a consequence of the limited mobility at the site. These adatoms then bond with further diffusing adatoms, whereby the cluster is formed and is energetically stable against diffusing across the surface, due to the collective number of bonds that would require to be broken and hence the large amount of work that would be required.

Moreover the image also displayed a rectangular surface vacancy which is presented more clearly within fig. 2.4b. It is uncommon to observe single adatoms or vacancies with an STM at room temperature due to their rapid propagation across the surface, however the vacancy of interest within fig. 2.4b is considerably large [3]. Briefly reiterating the discussion on such vacancies from section 1.5, the large nature of the vacancy is responsible for it being stable enough to image via STM whereas smaller surface vacancies would likely diffuse through terrace and not be observed[25]. Furthermore the two fold nature of this vacancy is a consequence of the atomic arrangement of the (100) surface of BCC structures. Elaborating, the vacancy most likely formed when two separate rows merged and left the sites of the vacancy shut off to diffusing adatoms, whereas the atoms at the kink had no energetic advantage for diffusing to most of the vacancies sites due to the inner wall of the vacancy offering the same coordination number as the kink itself.

Another interesting observation from data set A was the long range oscillation of wavelength $3.5 \pm 0.4\ nm$. As outlined within section 1.1.3, the wavelength of friedel oscillations from point defects if often of the order of several nm. Unfortunately the data at hand certainly doesn't permit the conclusion of the observation of such an oscillation. However it should be noted that further investigation into such an occurrence on the Ni-Al(100) will be required, as oscillations in the charge density of this nature may influence the functionality of the substrate as a template for the growth of Zn-Pc

---

[25] Refer to section 1.5 for clarification.

thin films.

3.2.2 Discussion of Zn-Pc Deposited Onto the Ni-Al(100) Surface

Successful deposition of the Zn-Pc molecule onto the Ni-Al(100) substrate was observed with a coverage of 0.05 ML, for an applied current to the thermal evaporator of 9.6 A. It was realised within the analysis that ~ 89 % of the molecules remain in-tact on the surface whereas the remaining 11 % fragment and distribute across the surface. The majority of the molecules were also observed to lie flat against the substrate, indicating that this is the energetically favourable orientation. Furthermore the molecules appear to align in two distinct orientation with respect to the substrate, however the precise nature of this orientation could not be determined due to the weak appearance of the substrate within the image of fig. 2.12.

Furthermore, no long range order was observed for coverage up to 1.88 ML, even after 20 minutes annealing at $\sim 400\ K$. It is noted however that this lack of long range order is specific to the conditions under which the investigation was performed and thus further investigation will be required. For example, the potential barrier for forming an rearranging into along range ordered structure may require annealing at a greater temperature. This was not yet clarified due to time constraints. Furthermore, the Zn-Pc molecules may form an ordered structure when deposited onto a substrate which is of higher or lower temperature than room temperature.

Finally, the Zn-Pc molecule has been successfully deposited onto the Ni-Al(100) substrate, however further investigation into the possibility of growing long range ordered thin films will be required for a wider range of experimental conditions.

Chapter 4

Conclusions and Future Work

4.1 Conclusions of the Work Presented

The Ni-Al complex metallic alloy and the Zn-Pc metal-organic semi-conductor are both materials of technological importance. The work presented employs UHV techniques to investigate the Ni-Al(100) surface and its viability as a substrate on which to grow Zn-Pc thin films.

The Ni-Al(100) surface was prepared with sputtering and annealing cycles, with the annealing at $\sim 800\ K$ which according to literature should result in a surface reconstruction. The implementation of LEED supported the formation of the expected $\mathrm{C}(\sqrt{2}\,\mathrm{x}\,3\sqrt{2})\mathrm{R}45°$ reconstruction. Furthermore the LEED data indicated a surface composition with equal parts Ni and Al distributed in an alternating diagonal row arrangement, in contradiction to the 1/3 Ni and 2/3 Al composition reported within the literature[1]. Moreover the corresponding surface arrangement was shown to also posses a P(3 x 3) unit cell which is again in contradiction to the reported P(2 x 2) unit cell. The disparity was considered to potentially be due to a different bulk composition between the samples used within the investigations, however the potential explanation was speculative.

Furthermore, STM data of the surface verified that the (100) plane experiences no ripple relaxation as is reported for the (110) and (111) surfaces and thus supporting the possible use of the (100) surface as a flat template for thin film growth. Moreover the (100) surface was observed to contain steps such that 76 % were between layers of like species and 14 % were between layers of different species based on the ideal bulk termination. Atomic resolution images of the surface displayed a long range oscillation of wavelength $3.5 \pm 0.4\ nm$, which were discussed inconclusively as potentially being an observation of Friedel oscillations.

The Zn-Pc molecule was successfully deposited onto the Ni-Al(100) substrate, displaying an energetic preference to lie flat against the substrate and to sit within one of two distinct orientations with respect to the substrate lattice, each of which with approximately equal frequency. However an estimated 11 % of the deposited molecules were observed to have fragmented upon deposition.

---

[1] Refer to chapter 1 for clarification.

Furthermore for coverage's ranging between 0.05-1.88 ML, no long range order was observed. The development of Zn-Pc thin films on the Ni-Al(100) substrate is thus an area of interest for further investigation.

4.2 Future Work and Closing Remarks

4.2.1 Continuation into Future Work

The work presented entails a preliminary investigation into the viability of the Ni-Al(100) surface as a template for Zn-Pc thin film growth. However the results of this investigation are not conclusive and in some instances may require further insight from investigation. An example of further work to be carried out is the use of x-ray diffraction to probe the composition of the bulk in order to determine whether the equal parts Al and Ni composition of the surface matches the stoichiometry of the bulk. This may help to elucidate the underlying cause of the contradictory results to those reported within the literature.

Furthermore the potential observation of friedel oscillations on the Ni-Al(100) surface was inconclusive, and thus the potential for the influence of such oscillations on thin film growth cannot be determined without further investigation. It would be beneficial for the associated investigation to be performed under lower pressure (10^{-11} $mbar$) and at low temperature (mK regime) in order to reduce all other excitations, noise and surface contaminant to more clearly distinguish the potential friedel oscillations.

Finally, it would be most instructive to investigate the Zn-Pc deposition over a range of substrate temperatures in order to determine whether a long range order of the resultant thin film may be observed.

4.2.2 Closing Remarks

During the period of the project, my contributions included; involvement with the experimental procedures and the collection of the raw data, the research into previous investigations of relevance, the analysis of all data presented within the thesis and all of the subsequent conclusions. However it must of course be acknowledged that conversations with those individuals mentioned within the acknowledgements section did have an influence on the line of analysis performed.

Appendices

List of Figures

List of Tables

Appendix A

Working With STM Images

STM images and moreover all spectroscopy images typically require an extent of manipulation in order to extract the required information. This is in part due to the precise nature of the experiment; that a small imperfection in the set-up may result in unwanted noise or an uneven sample surface. Thus the STM images presented within this work have typically undergone some image processing before any numerical values have been extracted. Where appropriate, such processing has been outlined so as not to mislead or misrepresent any facts to the reader; the processing relevant to this work is outlined and briefly explained with examples below.[1]

As outlined within section 1.6.1, the STM utilises a quantum mechanical tunneling current through a potential barrier. Additionally it was outlined in section 1.5 that adatoms on the surface can diffuse; in-fact they can often also be picked up[2] by the STM tip in response to the force produced by the biasing potential which is applied in order to produce a net tunneling current. Consequently, the conductivity of the tip can be reduced due to the shielding produced by the valance electrons of the contaminating atoms. The result is the horizontal[3] stripes that can be seen below in fig. A.1a, where there are sudden and incorrect variations in the mapped topography between consecutive scan lines. Similar noise signatures may be produced from external noise causing the tip to oscillate, however this is typically apparent as the resultant image will have a significantly greater and consistently distributed level of noise.

As can be seen within fig. A.1b, the consequence is that the height profile experiences high levels of noise; is not smooth and thus can be difficult to accurately extract numerical values from. It is also readily noticeable that the height profile reveals that the terraces were not flat[4] during the scanning.

---

[1] For further detail on the image processing used, the reader is guided towards [30].

[2] This is more so an issue when the biasing potential is negative, as the net current is from the sample surface to the STM tip, resulting in a higher probability of the tip attracting an adatom from the surface.

[3] They are aligned with the direction that the tip was scanning in, so in this instance the tip was scanning horizontally with respect to the resultant image.

[4] i.e. perpendicular to the length of the STM tip.

(a) Raw image.

(b) Height profile of the raw image.

Fig. A.1: STM data of the clean Ni-Al (100) surface.

The unwanted noise signatures are reduced by employing a flattening procedure, in which the software judges whether the variation of pixel value around each given point is to be taken as a genuine feature or as a noise signal. This is determined by considering the gradient of the pixel value around each point and assessing whether the variation is smooth and continuous[5]. Any pixels which are determined to be a component of a noise feature, have their pixel value altered as to provide a smooth and continuous pixel value gradient with respect to the surrounding pixels which have been determined to be genuine features. This flattening procedure is however also frequently used for correcting scan data for sample tilting. This is again achieved by considering whether variation[6] in the pixel values are genuine[7]. There are however three options within ImageJ$^{\text{TM}}$ for determining the required alteration in pixel value. The software will judge the correct variations using either; a constant offset, i.e. an average pixel value gradient determined based on the overall image; a line by line consideration, accounting for each line within the image[8] based on the local, rather than the global pixel value gradient; a parabolic fit, which takes the global pixel value data from the image and fits the variation to a parabola and uses this to determine the corrected values across the image. Within the example presented below in fig. A.2a, a flattening procedure was conducted utilising the line by line method. This clearly resulted in a significant level of noise reduction, as is supported in the corresponding height profile within fig. A.2b.

---

[5] Thus for a rapid change in pixel value along a given orientation, the variation may not be too short range or temporary, i.e. a sharp and very rapid increase followed by such a decrease. Such features are not genuine when over the length scales considered and may typically be accounted for by noise. Another consideration is whether the variation only occurs along a very narrow orientation, i.e. a along one particular direction but with no variation occurring slightly to the left or right of that orientation.

[6] However in this instance, the variation being considered by the software is longer range.

[7] This is arguably the main purpose for the flattening procedure, with the noise reduction simply being a secondary function or convenient capability.

[8] Which can be taken vertically or horizontally.

(a) Flattened line by line. **(b)** Height profile of the flattened image.

Fig. A.2: STM data of the clean Ni-Al (100) surface after a flattening procedure.

Unfortunately this height profile still exhibits terraces which do not appear to be flat, resulting in analysis being inaccurate. A procedure which is employed to account for this is a local plane. The local plane enables a renormalisation of pixel values within the image based on selecting various regions which are known to be of equal hight. The result for such a procedure which was carried out on the image within fig. A.2a is shown below in fig. A.3a, where the horizontal line at the top is the path over which the height profile was taken in all cases[9]. The pixel value clearly varies less dramatically and more smoothly across the individual terraces, with the terraces being more well defined and clearly distinguishable. The associated height profile presented in fig. A.3b shows flat terraces with better defined steps, enabling more accurate analysis of the data; in this case[10] being the step height.

(a) Additional local plane using the right terrace. **(b)** Height profile of the local planed image.

Fig. A.3: STM data of the clean Ni-Al (100) surface after both a flattening and local plane procedure.

Furthermore the order of implementation of the procedures presented above can influence the quality of the resultant image, and thus whenever data is presented within this work it should be understood that various approaches have been employed with the highest quality line of analysis being that which is presented and clearly outlined.

Noise reduction and sample tilting are also an issue within atomic resolution images such as that

---

[9] It has simply been omitted in the other two images.

[10] Given the absence of atomic resolution within this image.

shown below in fig. A.4a, where the atomic positions[11] are not clearly defined in parts of the image. Moreover there is an additional method of noise reduction[12] for images that achieve atomic resolution, in that a fast fourier transform (FFT) may be utilised to identify any periodicity within the image, an example of which is given in fig. A.4b.

(a) Raw image. **(b)** FFT of the raw image.

Fig. A.4: Atomic resolution STM data of the clean Ni-Al (100) surface.

Within the FFT image there are vertical and horizontal lines which are a result of the boundaries within the raw image, i.e. if the raw image could be made infinite in size then these lines would not be present [30]. There is however a caveat in that some of the vertical lines are a result of the noise produced by scanning[13] which was discussed above, which also elucidates the reason for there being more vertical lines than horizontal lines. Within the image there is also a central spot with four orbiting spots amidst a background of noise. The central spot is a feature of all FFT images and is an insignificant artifact, whereas the four orbiting spots are actually two spots which are being reflected through an axis running horizontally through the centre of the image. These spots correspond to repeated periodicity within the original image and in this instance reveal a 4-fold symmetry of the substrate. A reconstruction of the original image can be created which excludes all other elements of noise seen within the FFT other than the two spots, where the required procedure is an inverse fast fourier transform (IFFT) and an example corresponding to fig. A.4b is given below in fig. A.5a.

---

[11] It isn't quite that simple, as it is really the local density of states of the electrons that are being probed and thus it cannot be naively viewed in the same respect as an image from an optical technique.

[12] This isn't explicitly true as the periodicity being enhanced could in-fact be itself purely from a source of noise.

[13] The scanning direction was horizontal and thus the orientation within the FFT is rotated with respect to that in direct (real) space.

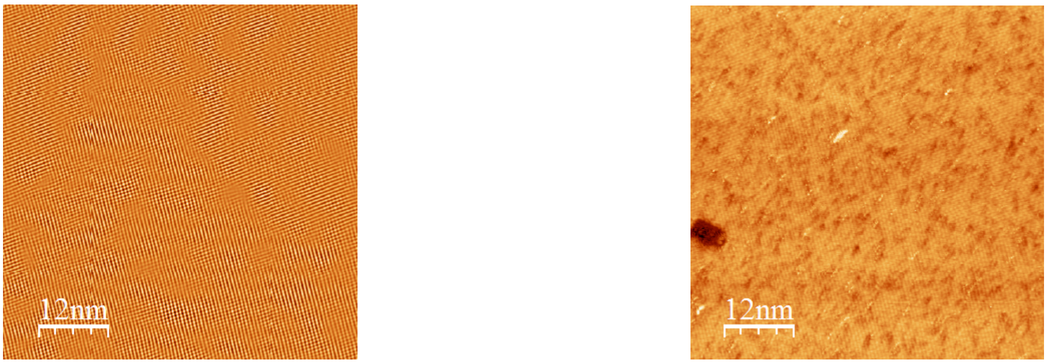

(a) IFFT of the raw image.

(b) Enhanced image (raw and IFFT merged).

Fig. A.5: Atomic resolution STM data of the clean Ni-Al (100) surface utilising a FFT procedure.

This IFFT can be merged with the original image in order to enhance the periodic features and deemphasise all other artifacts within the original image, as shown in fig. A.5b. The extent of enhancement is circumstantial to the original data and can be improved through using a flattening procedure before implementing the FFT.

Appendix B

Error Analysis and Determining Consistency

B.1 Error Analysis

The errors stated within the work presented have been calculated using a general expression for error propagation. For a given quantity A where;

$$A = B + CD \ , \tag{B.1}$$

then the associated error (dA) would be obtained from;

$$dA = \sqrt{\left(\frac{\partial A}{\partial B}dB\right)^2 + \left(\frac{\partial A}{\partial C}dC\right)^2 + \left(\frac{\partial A}{\partial D}dD\right)^2} \ , \tag{B.2}$$

where the error on each individual quantity is determined specifically for the present case, accounting for systematic and random error.

B.1.1 Error Determination for the LEED Data

The LEED data presented was analysed using the ImageJ$^{\text{TM}}$ software which presents the distance between two points within an image to a precision of 0.01 pixels. However the random human error associated with identifying the centre of the diffraction spots is approximately ±20 pixels at each measurement point, i.e. for a length measurement the total accumulated random error is;

$$dn = \sqrt{20^2 + 20^2} = \pm 28 \ . \tag{B.3}$$

Thus the precision error is relatively negligible, with the total error for the distance between two points within an image coming principally from the random error. The analysis included a conversion of the determined length values in order to account for a difference in scaling between the calibration data and the data of interest. Consequently there is thus a contribution from this conversion to the accumulated error for the length values. Employing eq. (B.2) it is readily understood that the error contribution is to multiply the initial random error by the scaling factor (a). Similarly the subsequent scaling to account for discrepancy in the zoom between the calibration image and the image of interest will contribute a constant factor (b) equal to that used within the scaling procedure. Reiterating the error accumulated thus far is;

$$dN = dn \cdot a \cdot b \ . \tag{B.4}$$

With the calibration image and the image of interest now scaled equivalently, the conversion from a pixel number (N) to a distance (A^*) was implemented using the scaling factor[1] (c) taken from the calibration data;

$$A^* = \frac{N}{c} \ , \tag{B.5}$$

with the associated error from employing eq. (B.2) of;

$$\begin{aligned} dA &= \sqrt{\left(\frac{\partial A^*}{\partial N} dN\right)^2 + \left(\frac{\partial A^*}{\partial c} dc\right)^2} \ , \\ &= \sqrt{\left(\frac{dN}{c}\right)^2 + \left(\frac{dc}{c^2}\right)^2} \ . \end{aligned} \tag{B.6}$$

Congruently, the final step of converting from reciprocal space to direct space via;

$$A = \frac{2\pi}{A^*} \ , \tag{B.7}$$

culminates in an error of;

$$dA = \frac{2\pi}{(A^*)^2} dA^* \ . \tag{B.8}$$

B.1.2 Error Determination for the STM Data

The error in the vertical position of the STM tip was previously calibrated to be ∼ 5 %. However as outlined in section 1.1.2, the NI-Al(100) has been observed under the preparation conditions applied within this work, to have Ni antisites within the Al surface layer [18]. Consequently the STM tip may potentially probe the electronic structure of two different species at the step between two terraces, thus not truly measuring the relative height of the two terraces. There is therefore an additional ∼ 10 % error incurred in the vertical position of the tip. Furthermore the horizontal tip positioning is subjected to ∼ 20 % as a consequence of the tip drifting during the scan.

Reiterating, the measurements made in the vertical orientation are subjected to an uncertainty of ∼ 15 %, whereas those made in the horizontal orientation are subjected to an uncertainty of ∼ 20 %.

---

[1] The error for the scaling factor c is equal to the error on a length measurement.

B.2 Determining Consistency

The consistency checks within this work between the presented results and any model or literature values, have been carried out using a prescription based on the formula;

$$\mid A - B \mid < \sqrt{(dA)^2 + (dB)^2} \ . \tag{B.9}$$

The premise is that if two values differ by an amount which is smaller than their combined error then those two values are consistent with one another to within one multiple of their total associated error. Two values are typically said to be consistent with one another if they lie within three multiples of their total associated error, however this discrimination is always most appropriately considered on a circumstantial basis.

Appendix C

LEED Calibration Data

The analysis presented within section 3.1 pertaining to the LEED data, required a calibration data set in order to scale between distance in the image and distance in the associated reciprocal space. A calibration scale was unambiguously determined by taking LEED data for the well understood Ag(100) surface, for which the preparation conditions required for bulk termination are known[1]. Consequently the ideally terminated Ag(100) surface provides a scale with which to utilise the data of interest. A model of the Ag(100) system was produced using the VESTA™ software and is presented below in fig. C.1.

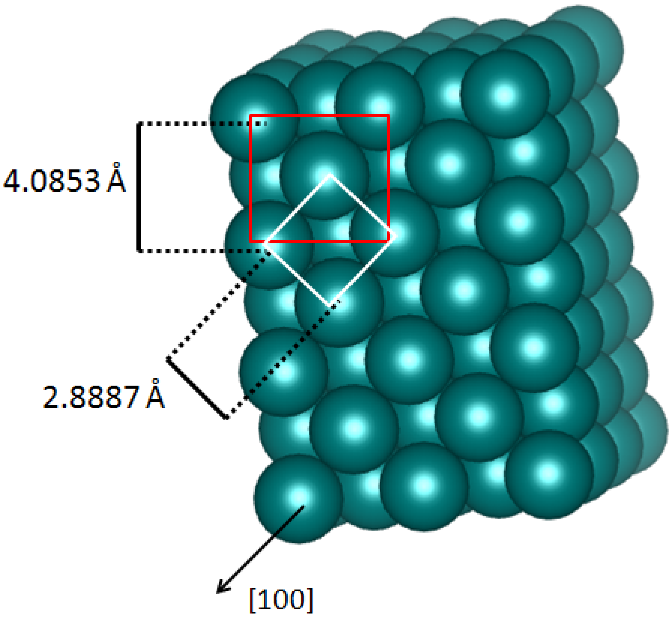

Fig. C.1: Showing a bulk model of Ag, with the primitive unit cell of the (100) plane shown in white and the smallest 4-fold non-primitive unit cell shown in red.

The data used for the calibration process is presented below in fig. C.2 and fig. C.3.

---

[1] In fact it is difficult to prepare Ag(100) in such a way that it does reconstruct, due to the d-orbitals undergoing significant d-s hybridisation [31].

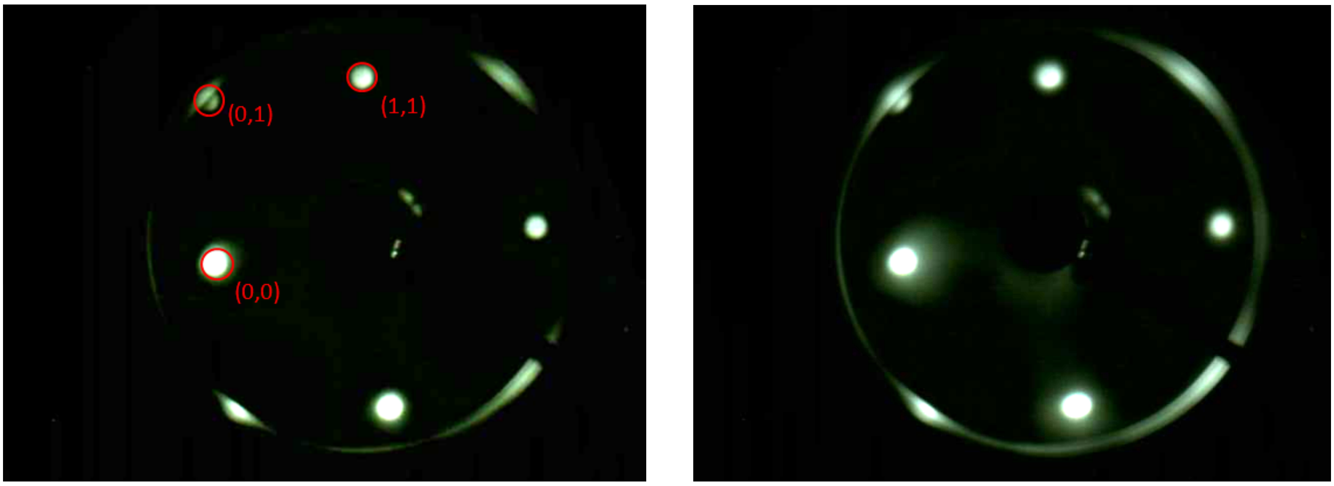

(a) Calibration data set 1. **(b)** Calibration data set 2.

Fig. C.2: Showing calibration data sets 1 and 2 taken with the Ag(100) surface.

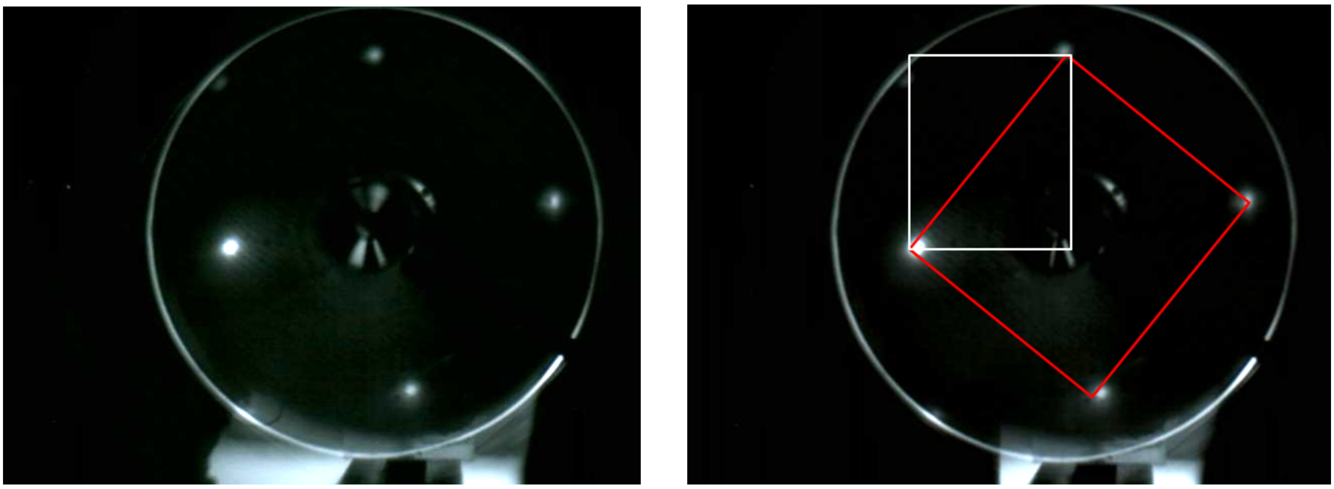

(a) Calibration data set 3. **(b)** Calibration data set 4.

Fig. C.3: Showing calibration data sets 3 and 4 taken with the Ag(100) surface.

These images have been manipulated to enhance their contrast in order to clearly distinguish the circumference of the fluorescent screen[2]. The same unit cells shown within fig. C.1 are displayed in fig. C.3b. Evidently the primitive unit cell of direct space translates into the primitive unit cell of reciprocal space, governed by the relation;

$$a_1 = \frac{2\pi}{a_1^\star} \, , \tag{C.1}$$

where a_1 and $a_1^\star$ are the real and reciprocal space lattice spacings respectively [3]. In the interest of error reduction, the principle measurements were taken[3] using the spacings of the unit cell shown in red in fig. C.3b due to the number of possible measurements available. The results are displayed below in table C.1.

---

[2] The associated diameter was used as a common feature of fixed size in order to account for differences in zoom between the data of interest and the calibration data, as outlined in section 3.1.

[3] The measurements were taken using the ImagaJ$^{\mathrm{TM}}$ software.

	Top Left (Pixels)	Top Right (Pixels)	Bottom Left (Pixels)	Bottom Right (Pixels)	Average (Pixels)
Dataset1	236.29	228.97	225.36	231.14	230.44
Dataset2	235.05	229.73	230.51	225.09	230.10
Dataset3	240.80	232.40	229.44	237.61	235.06
Dataset4	242.20	232.54	230.05	237.20	235.50
Final Value	/	/	/	/	232.78

Table. C.1: Showing the measurements of the length of the red unit cell outlined in fig. C.3b for the four calibration data sets.

Moreover, the lattice constant of the primitive unit cell shown in fig. C.1 was converted to a corresponding reciprocal space lattice constant via eq. (C.1), with a value[4] of 2.1751 $\AA^{-1}$. The subsequent spacing for the red unit cell of interest in fig. C.3b is given by an additional factor of $\sqrt{2}$ from pythagoras' theorem, incurring a value of 3.0760 $\AA^{-1}$.

Finally, a calibration scale may now be established by;

$$\frac{232.78 \text{ Pixels}}{3.0760 \ \AA^{-1}} = 75.68 \text{ Pixels } \AA.$$

Furthermore as outlined in section 3.1, the requirement to account for different levels of zoom between the image of interest and the calibration data necessitates a measurement for the diameter of the fluorescent screen, for use as a common feature. The results of these measurements with the calibration data, are tabulated below in table C.2.

	Horizontal (Pixels)	Vertical (Pixels)	Diagonal (Pixels)	Diagonal (Pixels)	Average (Pixels)
Dataset1	425.01	425.06	426.71	432.40	427.30
Dataset2	429.07	426.00	424.20	423.14	425.60
Dataset3	450.00	450.01	452.28	449.77	450.52
Dataset4	450.00	451.09	452.55	449.81	450.86
Final Value	/	/	/	/	438.57

Table. C.2: Showing the measurements for the diameter of the fluorescent screen, for the four calibration data sets.

---

[4] The units of reciprocal space are inverse length.

Bibliography

[1] M.Schwartz, *Encyclopedia of materials, parts and finishes, second edition.* CRC press, 2002.

[2] G.Torre *et al.*, *Functional Phthalocyanines: Synthesis, Nanostructuration, and Electro-Optical Applications.* Springer publishing, 2010.

[3] H. Ibach, *Physics Of Surfaces And Interfaces.* Springer publishing, 2006.

[4] C. Mudry, "Lecture notes on field theory in condensed matter physics," condensed matter theory group, Paul Scherrer Institute, Switzerland.

[5] J. Fraxedas, "Thin films of molecular organic materials," *Journal of Physics: Condensed Matter*, 2008.

[6] S.Senthilarasu *et al.*, "Characterisation of zinc phthalocyanine (ZnPc) for photovoltaic applications," *Applied physics A*, 2003.

[7] "Pubchem open chemistry database; searched for zinc phthalocyanine," https://pubchem.ncbi.nlm.nih.gov/compound/2735172, accessed 18/03/16.

[8] R.Theisen *et al.*, "Ground and excited states of zinc phthalocyanine, zinc tetrabenzoporphyrin, and azaporphyrin analogs using dft and tddft with franck-condon analysis," *Chemical physics*, vol. 142, 2015.

[9] O.Kaliya *et al.*, "Catalysis and photocatalysis by phthalocyanines for technology, ecology and medicine," *Journal of Porphyrins and Phthalocyanines*, 1999.

[10] D.Eley, "Phthalocyanines as semiconductors," *Nature*, 1948.

[11] T.Fleetham *et al.*, "Efficient zinc phthalocyanine/c_{60} heterojunction photovoltaic devices employing tetracene anode interfacial layers," *American chemical society Applied Materials & Interfaces*, 2014.

[12] L.Hammer *et al.*, "Segregation phenomena on surfaces of the ordered bimetallic alloy FeAl," *Surface Science*, 1998.

[13] J.Veen and M.Hove, *Springer Series in Surface Sciences 11 - The Structure of Surfaces II.* Springer publishing, 1987.

[14] J.Noonan *et al.*, “Mixture of ordered domains in the NiAl(111) surface,” *Physical review letters*, 1987.

[15] H.Overbury *et al.*, “Surface structure of stepped NiAl(111) by lowenergy Li+ ion-scattering,” *Surface Science*, 1990.

[16] R.Franchy *et al.*, “The adsorption of sulfur, carbon monoxide and oxygen on NiAl(111),” *Surface Science*, 1987.

[17] H.Overbury *et al.*, “The structure and composition of the NiAl (110) and NiAl (100) surfaces,” *Surface Science*, 1988.

[18] D.Lerch *et al.*, “Point defects in the Ni-Al(100) surface,” *Journal of condensed matter physics*, 2009.

[19] K.Hansen *et al.*, “Surface waves on NiAl(100),” *Physical Review B*, 2001.

[20] R.Blum *et al.*, “Preparation-dependent surface-composition and structure of NiAl(001) - spa-leed and niciss study,” *Surface Science*, 1996.

[21] B.Chatterjee *et al.*, “Screening of a single impurity and friedel oscillations in fermi liquids,” 2015.

[22] J. .Li *et al.*, “First-principle study of friedel oscillations normal to the low index surfaces of al,” *Physica B*, 2011.

[23] H.Lüth, *Solid Surfaces, Interfaces and Thin Films.* Springer publishing, 2015.

[24] S.Amelinckx *et al.*, *Diffraction and Imaging Techniques in Material Science - Volume II: Imaging and Diffraction Techniques.* North Holland publishing company, 1979.

[25] M.Mamonova *et al.*, *Surface Physics: Theoretical Models and Experimental Methods.* CRC press, 2014.

[26] M.Désjonqueres *et al.*, *Concepts in Surface Physics.* Springer publishing, 1993.

[27] S. Hufner, *Photoelectron spectroscopy: Principles and Applications.* Springer publishing, March 2013.

[28] A.Al-Mahboob *et al.*, “Interface energetics in zinc phthalocyanine growth on Ag(100),” *Physical Review B*, Submitted 2016.

[29] D.Mullins *et al.*, “The structure and composition of the NiAI(110) and NiAI(100) surfaces,” *Surface Science*, 1988.

[30] S. Barrett, *Image Analysis in Earth Sciences.* Springer publishing, 2014.

[31] A.Hubbard, *The Handbook of Surface Imaging and Visualization.* CRC press, 1995.